Geological Journal

Volcanic-plutonic connection and associated Au-Cu mineralization of the Tulasu ore district, western Tianshan, NW China: implications for mineralization potential in Paleozoic arc terranes

Journal:	*Geological Journal*
Manuscript ID	GJ-19-0493.R1
Wiley - Manuscript type:	Special Issue Article
Date Submitted by the Author:	19-Dec-2019
Complete List of Authors:	Zhao, Xiaobo; China University of Geosciences Beijing, State Key Laboratory of Geological Processes and Mineral Resources, Faculty of Earth Sciences and Resources; Natural History Museum, Center for Russian and Central Eurasian Mineral Studies, Department of Earth Sciences Xue, Chunji; China University of Geosciences Beijing, State Key Laboratory of Geological Processes and Mineral Resources, Faculty of Earth Sciences and Resources Seltmann, Reimar; Natural History Museum, Center for Russian and Central Eurasian Mineral Studies, Department of Earth Sciences Dolgopolova, Alla; Natural History Museum Andersen, Jens ; University of Exeter, Camborne School of Mines Zhang, Guozhen; China Geological Survey, Tianjin Center
Keywords:	Volcanic–plutonic connection, Tulasu epithermal ore district, Late Paleozoic arc magma, exploration potential, western Tianshan

SCHOLARONE™
Manuscripts

Volcanic-plutonic connection and associated Au-Cu mineralization of the Tulasu ore district, western Tianshan, NW China: implications for mineralization potential in Paleozoic arc terranes

Xiao-Bo Zhao[1,2,†], Chun-Ji Xue [1,†], Reimar Seltmann[2], Alla Dolgopolova[2], Jens C.Ø. Andersen[3], Guo-Zhen Zhang[4]

[1]State Key Laboratory of Geological Processes and Mineral Resources, Faculty of Earth Sciences and Resources, China University of Geosciences, Beijing 100083, China

[2]Center for Russian and Central Eurasian Mineral Studies, Department of Earth Sciences, Natural History Museum, Cromwell Road, London SW7 5BD, UK

[3]Camborne School of Mines, University of Exeter, Penryn Campus, Tremough, Penryn TR10 9FE, UK

[4]Tianjin Center, China Geological Survey, Tianjin 300170, China

Correspondence

Xiao-Bo Zhao or Chun-Ji Xue

State Key Laboratory of Geological Processes and Mineral Resources,

China University of Geosciences (Beijing), Beijing 100083, China.

Emails: xiaobozhao@cugb.edu.cn (X. Zhao), chunji.xue@cugb.edu.cn (C. Xue)

For Peer Review

ABSTRACT

Constructing the plutonic-volcanic connections in volcanic arc setting is essential for understanding a variety of magmatic processes from continental crust differentiation to formation of magmatic-hydrothermal ore deposits. Based on the combination of zircon U-Pb geochronology and Hf isotope and whole-rock geochemistry and Sr-Nd isotopes, we evaluated the potential connections between volcanic and plutonic rocks from the Tulasu basin, the largest epithermal gold ore district in the Chinese Western Tianshan. The peak of volcanism coincides well with the major plutonism, representing an important magma event at ca. 347–367 Ma. These contemporaneous volcanic and plutonic rocks show broadly similar arc-related geochemical signatures and zircon in-situ Hf ($\varepsilon_{Hf}(t)$=-1.0–14.3) and whole-rock Nd ($\varepsilon_{Nd}(t)$=-4.2–4.6) isotopic compositions, indicative of formation from parental magmas derived from a common depleted mantle source metasomatized by slab-derived melts, despite diverse consequent processes (fractional crystallization, crustal contamination and magma mixing/mingling) during their differentiation in a subduction-related setting. Volcanic rocks from the Axi caldera in the center of the Tulasu district are geochemically less evolved than the coeval porphyritic granite, which indicates that the intrusive rocks might originate from residual melts left behind by extraction of erupted magmas. In contrast, the porphyry Cu mineralized Kexiaxi pluton, which occurs in the margin of the Tulasu district, is compositionally indistinguishable from the coeval volcanic suites. This implies that the Kexiaxi pluton represents the intrusive equivalent of a common magma reservoir feeding the volcanic eruptions, and magma fluxes may

For Peer Review

have controlled their differentiation. We thus suggest that the depleted mantle derived calc-alkaline magma, modified during slab-related melt metasomatism, crustal contamination and magma mixing may have played an important role in copper enrichment at Kexiaxi. Finally, the relatively water-rich and fertile nature of arc magma of the Tulasu district indicates high exploration potential for significant porphyry Cu-Au deposits. The existing alteration-immobile fertility proxy (V/Sc) for intrusive rocks may also be useful to assess the fertility of cogenetic volcanic rocks, in turn with implications for unexposed porphyry Cu deposits at depths.

KEYWORDS

Volcanic–plutonic connection, Tulasu epithermal ore district, Late Paleozoic arc magma, exploration potential, western Tianshan

1. INTRODUCTION

Magmatic arcs host economically important porphyry Cu-Au and related epithermal Au deposits, which form through magmatic-hydrothermal processes in large and long-lived volcanic centers (Hollings, Cooke, & Clark, 2005; Nadeau, Stix & William-Jones, 2016; Sillitoe, 1973, 2010). Understanding the sources and petrogenetic evolution of arc-related volcanic and plutonic rocks hosting these deposits not only provide critical constraints on the volcanic arc development and continental crust differentiation, but also can better constrain the conditions conducive

For Peer Review

to the metal enrichment in the shallow crust. However, the relationships between erupted volcanic and intruded plutonic rocks is still a subject of ongoing debate (Annen, Blundy, Leuthold, & Sparks, 2015; Bachmann, Miller, & Silva, 2007; Glazner, Coleman, & Mills, 2015; Keller, Schoene, Barboni, Samperton, & Husson, 2015a; Lundstrom & Glazner, 2016). The 'crystal mush model' proposed by Bachmann & Bergantz (2004) has been used to explain the genesis of high-silica rhyolite and cogenetic plutonic suites in large, silicic magmatic systems. This model emphasizes physical processes of melt segregation from magma chambers, i.e., rhyolite forming by extraction of highly evolved melt from crystal mushes and intermediate magma mush piles left behind assembled incrementally to form plutons, hence resulting in complementary volcanic and plutonic compositions (Bachmann et al., 2007; Deering et al., 2016; Yan, He, Beier, & Klemd, 2018). By contrast, using global geochemical datasets, Glazner, Coleman, & Mills. (2015) indicated that plutonic and volcanic rocks in convergent margins are compositionally indistinguishable, and they further argued that magma fluxes might be the controlling factor of magma chamber processes, i.e., higher magma fluxes result in large volume eruption whereas plutons might be constructed incrementally over millions of years at lower magma fluxes (Annen, 2009; Caricchi, Annen, Blundy, Simpson, & Pinel, 2014; Glazner et al., 2015).

Devonian to Carboniferous volcanism are widespread in the northern Chinese western Tianshan, which constitute the northern active continental margin of the Yili Block and are suggested to have been formed in response to the southward subduction

For Peer Review

of the Junggar Ocean beneath the northern margin of the Yili Block (An, Zhu, Wei, & Lai, 2013; Wang, Faure, Shu, Cluzel, Charvet, De Jong & Chen, 2008; Xiao, Windley, Allen, & Han. 2013; Zhao, Xue, Chi, Wang, & Qi, 2014a; Zhu, Guo, Song, Zhang, & Gu, 2009). The Tulasu basin, situated in the western part of the Devonian-Carboniferous volcanic belt (Figure 1B), is to be known as the most important epithermal gold district in the Chinese western Tianshan (Chen, Pirajno, Wu, Qi, & Xiong, 2012; Yang, Mao, Bierlein, Pirajno, Zhao, Ye & Liu, 2009). The Axi caldera in the centre of the Tulasu distict hosts a series of major epithermal gold deposits (Axi, Tawuerbieke), and one porphyry Cu prospect (Kexiaxi) has been recently discovered at the northeastern margin of the district (Figure 1C). However, the relationships between the volcanic and plutonic rocks and their control on epithermal gold and copper porphyry mineralization of the district remain unanswered.

Previous studies on regional metallogeny suggested that the variable mineralization styles may have a close relationship, and further argued a high exploration potential for significant porphyry Cu-Au deposits of the Tulasu district (Peng, Gu, Cheng, Zhao, Wang, Lu & Han, 2018; Zhao et al., 2014a). This study presents new zircon U-Pb ages and Hf isotope and whole-rock geochemical and Sr-Nd isotope data for volcanic and plutonic rocks with an attempt to examine broader volcanic-plutonic links, magma sources and petrogenetic processes operating in the volcanic and plutonic realms and associated mineralization of the Tulasu district. This work advances the understanding of volcanic-plutonic parity and to aid

For Peer Review

regional prospecting of porphyry and related epithermal deposits in other volcano-plutonic belts.

2. GEOLOGICAL SETTING

The Chinese Western Tianshan in the southwestern Central Asian Orogenic Belt (Figure 1A) represents a Paleozoic orogenic collage that formed from multi-stage subduction-accretion of several terranes between the Tarim Craton and the Junggar Terrane (Figure 1B) (Charvet, Laurent-Charvet, Wang, Faure, Cluzel, Chen & De Jong, 2011; Gao, Li, Xiao, Tang, & He, 1998; Han & Zhao, 2018; Xiao et al., 2013). Its tectonic framework is marked by the three major suture zones, from north to south, namely the North Tianshan Suture, the Nikolaev-North Nalati Suture and the South Central Tianshan Suture (Figure 1B), which are considered to represent the Junggar, Terskey and South Tianshan oceans (Gao et al., 1998; Han & Zhao, 2018; Long, Gao, Klemd, Beier, Qian, Zhang & Jianget, 2011), respectively. These major sutures divide the Chinese Western Tianshan into four major tectonic domains, including the Chinese North Tianshan, the Yili Block, the Central Tianshan Block and the South Tianshan (Gao, Long, Klemd, Qian, Liu, Xiong, Su, Liu, Wang & Yang, 2009; Qian, Gao, Klemd, He, Song, Liu, Xu, 2009; Han, He, Wang, & Guo, 2011).

The Tulasu district is situated in the northern margin of the Yili Block (Figure 1B), and is hosted by an active continental margin formed due to southward subduction of the Junggar Ocean beneath the northern margin of the Yili Block (An et

For Peer Review

al., 2013; Wang et al., 2008; Zhu et al., 2009; Zhao et al., 2014a). The wedge-shaped Yili Block is regarded as the easternmost part of the Kazakhstan microcontinent (Biske & Seltmann, 2010; Windley, Alexeiev, Xiao, Kroner, & Badarch, 2007; Zonenshaĭn, Kuz′min, & Natapov, 1990). Its basement is composed of Meso- to Neoproterozoic marble and amphibolite facies metasedimentary and meta-igneous rocks (Liu, Wang, Shu, Jahn, & Lizuka, 2014; Wang, Liu, Shu, Jahn, Chung, Zhai & Liu, 2014a; Wang, Liu, Shu, Jahn, Chung, Zhai & Liu, 2014b), which crop out widely around the Sayram Lake (Figure 1B). These basement rocks are covered by late Neoproterozoic carbonates and Cambrian to Ordovician clastic and minor bimodal volcanic rocks (Gao et al., 1998; Liu et al., 2014), followed by extensive Devonian to Carboniferous arc-related volcano-sedimentary rocks along the northern and southern margins of the Yili Block (Figure 1B). Permian formations include the Early Permian bimodal volcanic rocks, and the Middle to Late Permian molasse deposition uncomfortably overlying the pre-Permian rocks (He, Zhang, Wang, Qian & Sun, 2018; Wang, Cluzel, Shu, Faure, Charvet, Chen, Meffre & De Jong, 2009). Voluminous Ordovician-Permian granitoids intrusions on both sides of the Yili Block (Figure 1B) were interpreted to be related to the subduction of the Junggar and / or South Tianshan oceans beneath the Yili Block (Huang, Long, Kröner, Yuan, Wang, Sun, Zhao & Wang, 2013; Long et al., 2011; Su, Cai, Sun, Wan, Wang, Bao & Xiao, 2018; Wang, Jahn, Shu, Li, Chung & Liu, 2012; Xu, Wang, Li, Chen, Ma, Zhu & Dong, 2013; Zhong, Wang, Alexeiev, Cao, Biske, Liu, Zhai & Xing, 2017).

For Peer Review

To the north, the Yili Block is separated from the Chinese North Tianshan by the North Tianshan Fault (Figure 1B). The Chinese North Tianshan consists mainly of Carboniferous volcano-sedimentary rocks, turbidites and tectonic enclosed ophiolite remnants (Gao et al., 1998), which are collectively interpreted as a late Carboniferous accretionary wedge formed by the southward subduction of the Junggar Ocean beneath the Yili Block (Gao et al., 1998; Wang, Zhao, Xu, Wyman, Xiong, Zi & Bai, 2006; Xiao et al., 2013). Biochronology of radiolarian chert and dating of gabbro (ca. 344 Ma) from the ophiolite mélanges indicate that the Junggar Ocean existed during Late Devonian-Early Carboniferous (Xiao, Tang, Feng, Zhu, Li & Zhao, 1992; Xu, Y., Li, Ma, Xia, Xia & Peng, 2006), and the ocean was closed in the Late Carboniferous (ca. 316–310 Ma) as evidenced by dating the Sikeshu stitching pluton that intruded into the ophiolite mélanges (Han, Guo, Zhang, Zhang, Chen & Song, 2010) and the Early Permian bimodal magmatism and olistostrome (Shu, Wang, Zhu, Guo, Charvet & Zhang, 2011) .

To the south, the Central Tianshan Block represents a continental ribbon that merged with the Yili Block along the Nikolaev-North Nalati Fault following the consumption of the Terksey Ocean in the middle Ordovician (Qian et al., 2009). It is composed predominantly of Neoarchean to Paleoproterozoic orthogneisses and metasedimentary rocks, and late Neoproterozoic to early Paleozoic carbonate–siliciclastic–volcanic successions (Gao et al., 2015; Wang et al., 2017; Xing, Zhao, Zhang, Ye, & Feng, 2016). These rocks are extensively intruded by Ordovician to Permian magmatic rocks as a result of the progressive closure of the South Tianshan

For Peer Review

Ocean and subsequent collision between the Central Tianshan Block and the Tarim Craton (Gao, Wang, Klemd, Jiang, Qian, Mu & Ma, 2009; Long et al., 2011; Zhong et al., 2017). The South Tianshan is a late Paleozoic accretionary complex bounded by the South Central Tianshan Suture to the north and the North Tarim Fault to the south (Figure 1B). The accretionary complex is mainly composed of the Kekesu-Akeyzi high-pressure metamorphic terrane, Silurian-Carboniferous ophiolite mélanges, as well as the imbricated late Ordovician to Carboniferous clastic and carbonate successions and early Paleozoic arc-related granitoids (Gao et al., 2009; Ge, Zhu, Wu, Zheng, Zhu & He, 2012; Xiao et al., 2013; Zhao, Zhang, Santosh, Huang, Cheng & Ye, 2015). Eclogite and blueschist from the Kekesu-Akeyzi terrane show consensus peak metamorphic ages at 320-310 Ma (Klemd, Bröcker, Hacker, Gao, Gans & Wemmer, 2005; Klemd, John, Scherer, Rondenay, & Gao, 2011; Li, Lin, Su, Li, Shi, Liu & Tang, 2011; Su, Gao, Klemd, Li, Zhang, Li, Chen & Zhang, 2010), which was interpreted to represent the approximate time frame for the collision between the Central Tianshan Block and the Tarim Craton, following the final closure of the South Tianshan Ocean (Gao et al., 2011; Han et al., 2011; Han & Zhao, 2018).

3. GEOLOGY OF THE TULASU AU-CU DISTRICT

Regionally, the Tulasu district is localized at the WNW-trending Tulasu basin bounded by the South Keguqin and North Yili basin faults (Figure 1C). The district represents a Paleozoic volcano-sedimentary basin developed on the Mesoproterozoic

http://mc.manuscriptcentral.com/gj

For Peer Review

and lower Paleozoic basements. The Mesoproterozoic basement consists mainly of neritic carbonate and siliciclastic rocks, whereas the lower Paleozoic basement comprises Middle Ordovician to Lower Silurian carbonate and calcareous siltstone with intercalated bimodal volcanic rocks at its lower part (XBGMR, 1993). These basement rocks are unconformably overlain by the sporadically preserved terrigenous molasse sequence of the Lower Devonian Tulasu Formation (Figure 1C), comprising conglomerate, pebbly sandstone, and siltstone. Early-middle Ordovician (480–450 Ma) volcanic gravels from the Tulasu Formation was assigned to represent the Ordovician rift-related bimodal volcanism (An, Zhu, Wei, & Lai, 2017). The widespread volcano-sedimentary succession of the Devonian to Lower Carboniferous Dahalajunshan Formation overlies the Tulasu Formation (Figure 2), and they are the principal host to major epithermal gold and zinc-lead deposits at the Tulasu district (Figures. 1C and 2). The Aqialehe Formation, which unconformably overlies the Dahalajunshan Formation, comprises mainly conglomerate, calcareous sandstone and mudstone (Figure 2). It was suggested to be Early Carboniferous based on numerous shallow-water fossils of *Siphonodendron sp*., *Caninia sp*. And *Gigantoproductus sp*. of the Visean stage (XBGMR, 1993). However, recent U-Pb dating of detrital zircons from the Aqialehe Formation have indicated a minimum depositional age of Early Permian (ca. 288 Ma) (Dong, Wan, Deng, Cai, & Xiao, 2018).

3.1 Dahalajunshan Volcanic Formation (DVF) and Related Epithermal Au Mineralization

For Peer Review

The DVF represents a series of calc-alkaline basaltic andesite to rhyolite arc volcanic successions and has a prolonged eruption history spanning from Early Devonian to Early Carboniferous (386–347 Ma), with most of the reported radioisotope ages concentrating to 367–347 Ma. (Figure 2) (An et al., 2013; Peng et al., 2018; Tang, Wang, Zhao, Wyman, Chen, Jia & Jiang, 2009; Zhai, Sun, Sun, Su, He & Wu, 2009; Zhao et al., 2014a; Zhao, Xue, Symons, Zhang, & Wang, 2014b). It encompasses dominantly andesitic to rhyolitic extrusive rocks interbedded with terrestrial sediments and relatively minored subvolcanic porphyritic andesite (An et al., 2013; Tang et al., 2009; Wang, Shu, Cluzel, Faure, & Charvet, 2007; Wang et al., 2009; Xia, Chen, Liu, & Luo, 2011; Zhao et al., 2014a). The extrusive successions, with a total thickness up to 1070–4500 m, were subdivided into five lithological members including, from base to top, the Conglomeratic, Acid tuff, Lower andesite, Volcaniclastic and Upper andesite members (XBGMR, 1993) (Figure 2). Among these, the uppermost member hosts a range of Paleozoic low-sulfidation epithermal Au (Axi, Tawuerbieke) and intermediate-sulfidation Zn-Pb deposits (Tabei), whereas the lower members (conglomeratic and acidic tuff) are host to high-sulfidation epithermal Au mineralization at Jingxi-Yelmend (Peng et al., 2018; Zhao et al., 2014a) (Figure 2).

The Axi area preserves a 2.6- × 2.4-km late Paleozoic maar-diatreme (Sha, Wu, Tian, Yang, & Jia, 1999) and associated ring and radial faults, where appear to have provided a favorable structural framework for emplacement of epithermal gold / zinc-lead veins forming the neighboring Axi, Tabei and Tawuerbieke deposits (Figure

For Peer Review

3A). The most significant deposit is the Axi low-sulfidation epithermal gold deposit, which contains estimated gold resources of ~2.3 Moz, averaging at 5.8 g/t (Rui, Goldfarb, Qiu, Zhou, Chen, Pirajno & Yun, 2002). Mineralization at the Axi deposit occurs as structurally-controlled veins within silicic and phyllic alteration zones, and is characterized by multiphase brecciation with fragments of both veins and disseminated host rocks (andesite and dacite) that are cemented by quartz ± calcite - sulfide veins (Zhai et al., 2009; Zhao et al., 2014a). Previously sensitive high-resolution ion microprobe (SHRIMP) dating has yielded U-Pb zircon ages of 356.2 ± 2.0 Ma and 363.2 ± 5.7 Ma for andesite and dacite (Zhai et al., 2009; An et al., 2013), respectively. A LA-ICP-MS zircon U-Pb date of 375.1 ± 3.6 Ma has been reported for zircons from a silicified andesite in the Axi deposit (Yu, Wang, Zhou, Xiao, & Yang, 2016).

Tawuerbieke is a small-sized gold deposit, which is mainly hosted by andesite and porphyritic granite that intruded into the Upper andesite member of the succession (Figure 3A). Gold mineralization comprises an early stage, low-grade, fracture-controlled type associated with pervasive quartz-sericite-chlorite-epidote-pyrite, and later overprinted by the auriferous quartz and carbonate veins (Zhao et al., 2014a). It is noteworthy that gold-mineralized monzonite porphyry and diorite enclaves hosted in silicified andesite have been recognized from the western Tawuerbieke area (Zhao et al., 2014b). Porphyritic granite intruding into the Upper andesite member occurs at the western Tawuerbieke area (Figure 3A). Tang et al. (2009) and Tang, Wang, Wyman, Sun, Zhao & Jiang.

For Peer Review

(2013) reported zircon U-Pb laser ablation inductively coupled mass spectrometry (LA-ICP-MS) ages of 347 ± 2 Ma and 349 ± 2 Ma for the andesite and the porphyritic granite, respectively. However, these ages are significantly younger than the U-Pb age of andesite (ca. 363 Ma) from the same member at the neighboring Axi deposit (Zhai, Sun, Gao, He, Liang, Miao & Wu, 2006). In contrast, zircon SHRIMP dating of the andesite and porphyritic granite yielded U-Pb ages of 361.0 ± 4.0 Ma and 355.4 ± 2.3 Ma (Zhao et al., 2014a), respectively. Moreover, a zircon U-Pb SHRIMP age of 356.2 ± 4.3 Ma from the monzonite porphyry enclave was reported (Zhao et al., 2014b).

Another major gold deposit in the Tulasu district is the Jingxi-Yelmend high-sulfidation epithermal deposit (1.6 Moz Au), which is ~ 6 km west-northwest from Axi (Figure 1C). Mineralization occurs preferentially at the unconformity between Ordovician limestone and the bottom of the DVF within silicic and advanced argillic alteration zones, with steeply-dipping post-ore faults cutting the ore horizon (Xiao, Nick, Graham, Fu, Wang & Pirajno; Zhao et al., 2014a). Zircon SHRIMP U-Pb ages of 386.4 ± 9.3 Ma has been reported for rhyolite and tuff from the bottom of the DVF (An et al., 2013), whereas subvolcanic porphyritic andesite from Jingxi-Yelmend area has U-Pb SHRIMP age of 370.5 ± 2.1 Ma (An et al. 2014).

3.2 Plutonic Rocks and Related Porphyry Cu Mineralization

Plutonic rocks are relatively minor outcropped within the Tulasu district (Figure 1C). Approximately 8 km northwest to Axi, the Kexiaxi composite intrusion

For Peer Review

represents the only porphyry Cu prospect at Tulasu (Figure 1C). The hypabyssal intrusion is oval in outcrop with dimensions of ~4.5 km^2, and intrudes into the Mesoproterozoic basement rocks of meta-clastic and limestone (Figure 3B). It comprises several intrusive phases, including gabbro diorite, quartz diorite, granodiorite, and diorite porphyry, with U-Pb zircon SHRIMP ages of 357.2 ± 3.0 Ma, 356.4 ± 2.2 Ma, 350.8 ± 3.8 Ma, and 348.0 ± 2.2 Ma (Xue, Wang, Zhao, & Chen. 2013), respectively. In contrast, Xie, Wu, Zhu, Zhong, Liu, Mei & Wang (2013) reported U-Pb zircon SHRIMP ages of 368.0 ± 5.2 Ma and 354.0 ± 4.1 Ma for the gabbro diorite and granodiorite, respectively.

Copper porphyry mineralization of the Kexiaxi pluton is characterized by a barren potassic core developed in granodiorite, and phyllic zone marked by abundant Cu-bearing quartz veinlets and epidote zone associated with minor Mo mineralization, followed by late chlorite-carbonate zone that affected all the intrusive phase (Xue et al., 2013; Zhao et al., 2014a). Previous whole-rock geochemical data suggested that the four intrusive phases share similar arc-related geochemical affinities (Xie et al., 2013; Xue et al., 2013).

4. SAMPLING AND ANALYTICAL METHODS

4.1 Sampling

Fieldwork and sampling for this study were designed to complement published datasets of volcanic and plutonic rocks mainly around the Axi-Tawuerbieke and

For Peer Review

Kexiaxi deposit area (Tables 1 and 2). We have analyzed forty-one samples (12 volcanic and 29 plutonic rocks) for whole-rock Sr-Nd isotopes, and eight samples (2 volcanic and 6 plutonic rocks) were chosen for zircon Hf isotope analysis. Twelve volcanic rock samples were analyzed for whole-rock geochemistry, whereas 1 andesite from Axi and another 1 porphyritic granite from Tawuerbieke for U-Pb zircon dating. Sampling information and petrological descriptions of the studied igneous rocks are presented in Tables 1 and 2. The locations of the dated samples are also shown in Figure 3, and representative field photographs and photomicrographs of samples are depicted in Figure 4.

4.2 Analytical Methods

Zircon grains were handpicked under a binocular microscope after conventional crushing, grading, magnetic and heavy liquid separation. Selective zircon grains were mounted in an epoxy resin (along with the standard zircon SL13 and TEMORA 1 for the SHRIMP mounts), and polished to expose the grain centers. To reveal their internal texture and to select spots for U-Pb dating, polished mounts were imaged by transmitted and reflected light, and by cathodoluminescence (CL).

Zircon U-Pb isotopic analyses for the sample TWE-35 (porphyritic granite) was conducted using the SHRIMP II ion microprobe at the Beijing SHRIMP center, Chinese Academy of Geological Sciences, following the analytical procedures described by (Williams, 1998). Standard zircon SL3 (U = 238 ppm) (Williams, 1998)

http://mc.manuscriptcentral.com/gj

For Peer Review

and TEMORA 1 ($^{206}Pb/^{238}U$ age = 417 Ma) (Black, Kamo, Allen, Aleinikoff, Davis, Korsch & Foudoulis, 2003) were used to calibrate measured element abundance and $^{206}Pb/^{238}U$ ratios, respectively. Common Pb correction was applied using measured ^{204}Pb and data reduction were performed using the SQUID 1.0 and Isoplot 3.00 programs (Ludwig, 2003).

LA-ICP-MS zircon U-Pb dating for the sample AX-2 (andesite) was carried out using an Agilent 7500a ICP-MS equipped with a 193-nm ArF-excimer laser housed at the State Key Laboratory of Continental Dynamics in Northwest University, Xi'an, China. Standard zircon 91500 was used as the external standard for the age calculation, and the NIST SRM 610 as an external standard for the calibration of U-Th-Pb concentrations in conjunction with the internal standardization using ^{29}Si. Common Pb was evaluated following the method proposed by Andersen (2002). Age calculations and plotting of Concordia diagram were performed using the Isoplot 3.00 program (Ludwig, 2003). Uncertainties for individual analyses are quoted at the 1σ level, whereas errors for weighted mean age at the 2σ level (with 95% confidence).

Whole-rock major element oxides were analyzed on powdered samples at the Chemical Laboratory of the Beijing Research Institute of Uranium Geology (BRIUG) by X-ray fluorescence (XRF) spectrometry (Philips PW2404) with analytical errors less than 5%. Trace elements were measured by ICP-MS using a Finnigan MAT-6493 (Element I) instrument in the same laboratory. The analytical accuracy and precision were generally better than 2–5%, estimated from repeated analyses of the Chinese

For Peer Review

National standards GBW 07106 and GBW 07312. Detailed analytical procedures were described in (Cullen, Field, & Sherrell, 2001).

Whole-rock Sr-Nd isotopic compositions were determined using an ISOPROBE-T thermal ionization mass spectrometer (TIMS) at the Isotope Laboratory of BRIUG. Powder sample was dissolved in a mixture of HF-HNO_3-$HClO_4$ in sealed Teflon capsules on a hot plate for 24 hours. After the separation of the Rb, Sr, and light REE in a cation-exchange column, the Sm and Nd were further purified using a cation-exchange column, conditioned and eluted with dilute HCl. Repeated analyses of the NBS987 Sr reference standard yielded $^{86}Sr/^{88}Sr$ = 0.710250 ± 0.000007 (2σ), and the SHINESTU Nd reference standard yielded $^{146}Nd/^{144}Nd$ = 0.512118 ± 0.000003 (2σ). The Sr and Nd isotopic fractionation was corrected to $^{87}Sr/^{86}Sr$=0.1194 and $^{143}Nd/^{144}Nd$=0.7219, respectively. Total chemical blanks were < 200 pg for Sr and < 50 pg for Nd. The $^{87}Rb/^{86}Sr$ and $^{147}Sm/^{144}Nd$ ratios were calculated using the Rb, Sr, Sm, and Nd abundances measured by ICP-MS.

In situ zircon Lu-Hf isotopic compositions were measured on the same zircon grains, previously analyzed for U-Pb SHRIMP and LA-ICP-MS isotopes (Figure 5). Lu-Hf isotopic analyses were conducted using a Nu Plasma multi-collector ICP-MS equipped with a 193-nm ArF-excimer laser at the State Key Laboratory of Continental Dynamics in Northwest University, Xi'an, China. Detailed instrumental conditions and analytical procedures were described by (Yuan, Gao, Dai, Zong, Günther, Fontaine & Diwu, 2008). Standard zircons 91500, GJ-1 and Monastery were used to monitor the instrumental stability and accuracy. During analyses, the $^{176}Hf/^{177}Hf$

For Peer Review

ratios for standards GJ-1 and Monastery standards were 0.282023 ± 0.000011 (2σ, n = 36) and 0.282727 ± 0.000007 (2σ, n = 36), which are comparable within errors to recommended values of 0.282015 ± 0.000019 (2σ) for GJ-1 (Elhlou, Belousova, Griffin, Pearson, & O'Reilly, 2006) and 0.282738 ± 0.000004 (2σ) for Monastery (Woodhead & Hergt, 2005), respectively. The ^{176}Lu decay constant of 1.865×10^{-11} yr^{-1} (Scherer, Münker, & Mezger, 2001), the chondritic parameters of $^{176}Hf/^{177}Hf = 0.282772$ and $^{176}Lu/^{177}Hf = 0.0332$ (Blichert-Toft & Albarède, 1997) were used to calculate initial $^{176}Hf/^{177}Hf$ ratios and $\varepsilon_{Hf(t)}$ values. Calculation of one-stage Nd model ages (T_{DM1}) was based on a depleted mantle source with the present-day $^{176}Hf/^{177}Hf$ ratio of 0.28325 and $^{176}Lu/^{177}Hf$ ratio of 0.0384 (Griffin, Pearson, Belousova, Jackson, Van Achterbergh, O'Reilly & Shee, 2000). The two-stage model ages (T_{DM2}) were calculated by referring to a $^{176}Lu/^{177}Hf$ ratio of 0.015 for the average continental crust, that originated from the depleted mantle source (Griffin, Wang, Jackson, Pearson, O'Reilly, Xu & Zhou, 2002).

5. RESULTS

5.1 U-Pb Zircon Geochronology

Zircon grains from both the porphyritic granite (#TWE-35) and the andesite (#AX-2) display euhedral to subhedral shapes, concentric oscillatory or sector zoning with minor grains show indications of xenocrystic cores and younger overgrowth rims. Xenocrystic cores were avoided whenever possible during analysis. Representative

For Peer Review

CL images for the dated zircon grains are presented in Figure 5 along with the spot locations and isotopic data of U-Pb and Hf. The U-Pb isotopic data are listed in Supplementary Table DR1 and illustrated on Concordia diagrams in Figure 6.

Twenty SHRIMP U-Pb analyses were carried out on 20 zircon grains from porphyritic granite #TWE-35. Except for one spot with relatively low value of 0.1, Th/U ratios of all the other analyses are in the range of 0.4–1.1. Seven spot analyses of the twenty analyses give older ages ranging from 390.8 to 484 Ma and are likely xenocrysts. The remaining thirteen individual spot analyses from fourteen separate zircon grains yielded a mean $^{206}Pb/^{238}U$ age of 356.0 ± 4.0 Ma (mean square of weighted deviates [MSWD] = 0.33; Figure 6A).

Twenty-one LA-ICP-MS U-Pb analyses were undertaken on 21 zircon grains from andesite #AX-2. Their Th/U ratios vary from 0.4 to 1.2. All the 21 analyses have indistinguishable $^{206}Pb/^{238}U$ ages and district on the Concordia with a weighted mean $^{206}Pb/^{238}U$ age of 351.1 ± 1.8 Ma (MSWD = 0.13; Figure 6B).

5.2 Major- and Trace-Element Compositions

Our 12 new whole-rock major and trace element geochemical results on volcanic rocks, were combined with previously published dataset of 40 volcanic and 53 plutonic rocks from the Tulasu district (Supplementary Table DR2). The host rocks (DVF) of epithermal gold deposits at Axi, Tawuerbieke and Jingxi-Yelmend comprise mostly hydrothermally altered volcanic rocks, range from basaltic andesite to rhyolitic

For Peer Review

compositions (SiO_2 = 51.54–74.10 wt.%; Figure 7A). Plutonic rocks, including the composite intrusion hosting the Kexiaxi porphyry Cu prospect and porphyritic granite associated with epithermal gold mineralization at Tawuerbieke, spanning the compositional range between gabbroic diorite to granite (SiO_2 = 50.98–77.15 wt.%; Figure 7A). These samples possess variable loss on ignition (LOI) values, with the volcanic rocks extending to higher LOI (2.0 to 10.7 wt.%) compared to bulk of the intrusive rocks with LOI values < 3.0 wt.% (Supplementary Table DR2). Classification based on immobile element ratios of Zr/TiO_2 and Nb/Y (Winchester & Floyd, 1976) indicates a compositional range from basaltic andesitic to dacitic for the igneous rocks at Tulasu (Figure 7B). On the Th–Co diagram (Hastie, Kerr, Pearce, & Mitchell, 2007), the majority of the volcanic and plutonic rocks are calc-alkaline with a few being high-K calc-alkaline and shoshonitic composition (Figure 7C). Binary plots of the volcanic and plutonic rocks for most of the major elements show a linear correlation with SiO_2 (Figure 8), however, the Tawuerbieke intrusive rocks display the highest concentrations of SiO_2 (72.68–77.15 wt.%), and tend to lower concentrations of CaO, $Fe_2O_3^{(t)}$, MgO, P_2O_5, Al_2O_3 and incompatible trace elements of Sr, Y, V and Sc (Figure 8). In contrast, samples from the Kexiaxi pluton show a compositional gap between 56–64 wt.% SiO_2, and trend to higher overall P_2O_5, Al_2O_3, MgO and incompatible elements (Figure 8).

The volcanic and plutonic rocks at the Tulasu district show comparable primitive mantle-normalized trace and chondrite-normalized rare earth element (REE) patterns (Figure 9), with enrichment in large-ion lithophile elements (LILE) of Rb, Ba, Th and

For Peer Review

U, and depletion in Nb and Ta. REE concentrations of these igneous rocks display variable enrichment in light REE for the volcanic (La_N/Yb_N = 2.16–21.58 with an average of 6.75) and plutonic rocks (La_N/Yb_N = 2.47–11.70 with a mean of 6.10), respectively, with no or minor negative to positive Eu anomalies (Eu/Eu* = 0.49–1.09, with an average of 0.84 for the volcanic rocks, and 0.67–1.42, with a mean of 0.89 for the plutonic rocks) and flat to slightly depleted heavy REE with mean Gd_N/Yb_N values of 1.40 and 1.31 for the volcanic and plutonic rocks (Supplementary Table DR2), respectively.

5.3 Sr-Nd Isotopic Data

The age-corrected whole-rock Sr-Nd isotopic data for the igneous rocks from the Axi-Tawuerbeike and Kexiaxi deposit area are listed in Supplementary Table DR3 and presented in Figure 10A. Twelve samples of the volcanic rocks (DVF) and 6 near contemporaneous plutonic rocks associated with epithermal Au mineralization at Axi-Tawuerbieke exhibit nearly identical Sr-Nd isotopic compositions, which are characterized by relatively low initial $^{87}Sr/^{86}Sr$ ratios of 0.70386–0.70702, near zero to slightly positive $\varepsilon_{Nd}(t)$ values of -1.0 to 2.0 and two-stage Nd isotope depleted mantle model ages (T_{DM2}) ranging from 949 to 1180 Ma. By contrast, the twenty-three plutonic rock samples from the Cu-bearing Kexiaxi composite intrusion display highly variable Sr-Nd isotopic compositions (Figure 10A), and are characterized by

For Peer Review

higher initial $^{87}Sr/^{86}Sr$ ratios of 0.70484–0.70828, low negative to high positive $\varepsilon_{Nd}(t)$ values from -4.2 to 4.6 with T_{DM2} varying from 726 to 1445 Ma.

Nine samples from the gabbro diorite, the earliest intrusive phase of the Kexiaxi composite pluton, have initial $^{87}Sr/^{86}Sr$ ratios of 0.70484–0.70807 and $\varepsilon_{Nd}(t)$ values ranging from -1.3 to 1.3 (Figure 10A). However, five samples each for the second (quartz diorite) and third (granodiorite) phase of the Kexiaxi pluton show narrow ranges of initial $^{87}Sr/^{86}Sr$ ratios (0.70626–0.70681 for quartz diorite and 0.70749–0.70828 for granodiorite), with low negative $\varepsilon_{Nd}(t)$ values of -4.0 to -3.4 and -4.2 to -2.2, respectively. Initial $^{87}Sr/^{86}Sr$ ratios of the four diorite porphyry samples, which form the last intrusive phase of the Kexiaxi pluton, are from 0.70575 to 0.70771, together with high positive $\varepsilon_{Nd}(t)$ values range from 3.6 to 4.4 (Figure 10A).

5.4 Zircon Lu-Hf Isotopic Data

In situ zircon Lu-Hf isotope data of the igneous rocks from the Axi-Tawuerbeike and Kexiaxi deposit area are listed in Supplementary Table DR4 and plotted in Figure 10B. Synmagmatic zircon grains of two andesite samples from the DVF (#AX-2 and #TWE-20) at Axi-Tawuerbieke yield $^{76}Hf/^{177}Hf$ ratios of 0.282536–0.282910, with $\varepsilon_{Hf}(t)$ values ranging from -0.9 to 12.1 and two-stage Hf isotope depleted mantle model ages (T_{DM2}) from 581 to 1174 Ma (n = 40). In addition, two porphyritic granite samples (#TWE-8 and #TWE-35) samples from the Axi-Tawuerbieke area exhibit undistinguishable zircon Lu-Hf isotopes compositions ($^{176}Hf/^{177}Hf$ = 0.282533–

For Peer Review

0.282968, $\varepsilon_{Hf}(t)$ = -1.0–14.3, T_{DM2} = 446–1425; n =23) with their near contemporaneous volcanic host rocks.

Synmagmatic zircon grains from the four dated intrusive phases (gabbro diorite, quartz diorite, granodiorite and diorite porphyry) of the Kexiaxi pluton (KXX-23, KXX-11, KXX-33 and KXX-14) display $^{176}Hf/^{177}Hf$ ratios from 0.282591 to 0.282860, positive $\varepsilon_{Hf}(t)$ values from 1.2 to 10.6, and variable depleted mantle model ages (T_{DM2}) from 687 Ma to 1281 Ma (n = 59).

6. DISCUSSION

6.1 Effects of Alteration on Whole-Rock Geochemistry

Samples of the Dahalajunshan volcanic Formation from this study and the literature were mostly collected close to low- and high-sulfidation epithermal gold districts, and it was inevitable that some of them undergone alteration overprint, which also revealed in their elevated LOI (>3 wt. %) and the variable silicic, sericite and chlorite alteration (Figs. 4D and 4E). This raises a necessity to assess the alteration intensity of effects on the whole-rock geochemical data. Based on a number of studies, it is generally accepted that selected major elements (P, Ti, Mn), high field strength elements (HFSEs), as well as transitional (Cr, Co, Ni, V, Sc) and rare earth elements (REEs; except Ce and Eu) are relatively immobile during hydrothermal alteration (Winchester & Floyd, 1976; Hastie et al., 2007), whereas alkali elements (Ca, Na, K)

For Peer Review

and some large ion lithophile elements (LILEs), especially Sr, Rb, Ba and Cs are highly mobile during alteration (Rollinson, 1993).

On the alteration box plot (Williams & Davidson, 2004), which is effective to quantitatively evaluate whole-rock chemical modification due to alteration in porphyry and epithermal settings, the majority of the Tulasu volcanic and plutonic rocks falls within or close to the unaltered box defined by (Large, Allen, Blake, Herrmann, 2001) (Figure 11A). However, alkali major elements (K, Ca, Na, Al) and LILEs (Rb, Ba, Sr, Y) of these samples display variable degrees of scatter when plotted against SiO_2 (Figure 8), which may be caused by post-magmatic hydrothermal alteration, in particularly the alteration and breakdown of plagioclase, clinopyroxene, sericite and chlorite (Rollinson, 1993). In contrast, selected major elements of $Fe_3O_4^{(total)}$, MgO and P_2O_5, and transitional metals (V, Sc) exhibit coherent trends with limited scatter on variation diagrams (Figure 8), together with the overall smooth and coherent patterns of chondrite-normalized REE and most HFSEs (Th, Nb, Ta, Zr, Hf) on the primitive mantle-normalized trace element diagrams (Figure 9), suggesting that these elements remain largely immobile during hydrothermal alteration, reflecting the original compositions of these rocks.

For the whole-rock Sr-Nd isotopic data of this study, the analyzed samples show variable and relatively large scatter of the $^{87}Sr/^{86}Sr_{(i)}$ values (Figure 11B), which should at least partially reflect alteration processes, rather than magmatic compositions and, hence, will not be employed in the following discussions. However, the $\varepsilon_{Nd}(t)$ and $^{143}Nd/^{144}Nd_{(i)}$ values of all the analyzed samples are

http://mc.manuscriptcentral.com/gj

For Peer Review

consistent for a given rock type (Table 1), and they also show no clear trend with the corresponding LOI value (Figs. 11C and 11D), indicating minimal effects of hydrothermal alteration on the Nd isotopic system, and hence can be used to identify the magmatic petrogenesis and assess the magma fertility.

6.2 Petrogenetic Processes and Magma Source Characteristics

6.2.1 Fractional Crystallization with Crustal Contamination and Magma Mixing

The DVF and plutonic rocks at the Tulasu district show igneous rock associations of basaltic andesite, andesite, rhyolite, gabbro diorite, quartz diorite, granodiorite, diorite porphyry, and porphyritic granite (Figure 3). Previous whole-rock geochemistry studies on these rock suites have identified many similarities, such as calc-alkaline in composition, LILE and light REE enrichment, negative Nb, Ta, and Ti anomalies (Figure 9), and broadly similar ages with regional arc-related magmatism along the northern Yili Block (An et al., 2013; Long et al., 2011; Tang et al., 2009, 2013; Wang et al., 2006, 2007, 2008, 2009; Xia, Chen, Liu & Luo, 2011; Xie et al., 2013; Xue et al., 2013). However, these contemporaneous volcanic and plutonic rocks have narrow variability in some trace elements and distinct Sr-Nd isotopic compositions (Figs. 8 and 10A), and thus are not related by any closed system processes. Petrogenetic processes such as fractional crystallization, crustal contamination, magma mixing/mingling may have been involved during the magma evolution (Kemp, Hawkesworth, Foster, Paterson, Woodhead, Hergt, Gray & Whitehouse, 2007).

For Peer Review

Decreasing CaO, $Fe_2O_3^{(t)}$, MgO, P_2O_5, Al_2O_3 with increasing SiO_2 concentrations in the Tulasu volcanic and plutonic rocks (Figure 8) are consistent with fractional crystallization, which is supported by phenocryst assemblage of plagioclase, clinopyroxene and amphibole in both rock suites (Figure 4). Moreover, the nearly constant Tb/Yb ratios with increasing Yb contents (Figure 12A) also suggest that fractional crystallization may have controlled the compositional variations within the suites (Fan, Guo, Wang, & Zhang, 2004). The concave-shaped chondrite-normalized REE patterns (Figure 9), decreasing Dy/Yb ratios with SiO_2 (Figure 12B), and lack of significant negative Eu anomalies imply a dominant amphibole fractionation and suppression of early fractionation of plagioclase (Davidson, Turner, Handley, Macpherson & Dosseto, 2007). Increasing Na_2O and decreasing CaO, Al_2O_3, and Sr with magma differentiation (Figure 8) are consistent with late crystallization of alkali-rich minerals (e.g., plagioclase) in relatively shallow crust levels (Hora, Singer, Wörner, Beard, Jicha & Johnson, 2009).

The presence of Neo- to Paleo-Proterozoic inherited zircon grains (756–1996 Ma) in the Tulasu volcanic and plutonic rocks (An et al. 2014; Xie et al., 2013) indicates that crust contamination/assimilation could have played a role during their evolution. This conclusion is also supported by the relatively wide range of Hf isotopic compositions in the synmagmatic zircon grains (Figure 10B). Given that the crustal rocks have relatively high $^{87}Sr^{86}Sr$ and low $\varepsilon_{Nd}(t)$ values, their assimilation in parental magmas would result in elevated $^{87}Sr^{86}Sr$ and lower $\varepsilon_{Nd}(t)$ values, decreasing $\varepsilon_{Nd}(t)$ with magma evolution, as well as negative correlation of $^{143}Nd/^{144}Nd_{(i)}$ with

For Peer Review

$^{147}Sm/^{144}Nd$ (DePaolo, 1981). In this study, volcanic and contemporaneous plutonic rocks from Axi-Tawuerbieke show generally constant trends in $^{143}Nd/^{144}Nd_{(i)}$ vs. $^{147}Sm/^{144}Nd$ and $\varepsilon_{Nd}(t)$ vs. SiO_2 plots (Figures. 12C and 12D), suggesting limited crustal contamination during their ascent and emplacement.

Conversely, data for the Kexiaxi pluton, except for the diorite porphyry, display negative correlation of $\varepsilon_{Nd}(t)$ with SiO_2 (Figure 12C), as well as in $^{143}Nd/^{144}Nd_{(i)}$ vs. $^{147}Sm/^{144}Nd$, documenting a significant role of crustal contamination. Samples from the Kexiaxi diorite porphyry show distinct Nd isotopic compositions ($\varepsilon_{Nd}(t)$ = 3.6–4.4) with samples from all the other intrusive phases ($\varepsilon_{Nd}(t)$ = -4.2–1.3) from the same pluton, showing positive correlations of $\varepsilon_{Nd}(t)$ with magmatic evolution (Figure 12C). Such characteristics can be explained by magma mixing/mingling processes, which is consistent with the presence mafic microgranular enclaves (MMEs) in the Kexiaxi granodiorite (Figure 4H), as well as the disequilibrium textures, such as oscillatory zoning, sieve and honeycomb textures of plagioclase crystals in the Kexiaxi pluton (Figure 4I-L). The MMEs display transitional contact with their host granodiorite and are spheroidal to ellipsoidal in shape with equigranular and fine-grained textures (Figure 4H), supporting they are globules of mafic melts that were injected into the host felsic magma. Xenocrysts of plagioclase and quartz in the MMEs (Figure 4H) also indicate that they are mechanically incorporated into the mafic magma possibly during the magma mixing processes (Hibbard, 1981). All these characteristics, hence, suggest the involvement of crustal components and magma mixing/mingling during ascent and emplacement of the Kexiaxi pluton into the crust.

For Peer Review

6.2.2 Magma Sources

Existing geochronological data and our new age data collectively indicate broad contemporaneity between volcanic and intrusive rocks in the Tulasu district (Table 2), defining a magma flare-up to have occurred at ca. 347–367 Ma. These late Devonian to early Carboniferous igneous rocks are mainly calc-alkaline in composition and belong to I-type magmas, sharing similar abundances of major and trace elements with the compiled continental igneous rock datasets globally (Keller et al., 2015b). Based on their lithological association, mineral assemblages and subduction-related geochemical signatures, these rocks were suggested to have been generated in a supra-subduction setting, which was related to the southward subduction of the Junggar Ocean beneath the northern margin of the Yili Block (An et al., 2013; Peng et al., 2017; Tang et al. 2009, 2013; Xie et al., 2013; Xue et al. 2013; Zhao et al., 2014b;), forming the eastern part of the Devonian to Carboniferous Balkhash-Yili Andean-type magmatic arc belt (Windley et al., 2007; Xiao & Santosh, 2014).

Whole rock geochemistry shows that these volcanic and plutonic rocks are either featured with typical continental arc magma signatures (An & Zhu, 2008; An et al., 2013; Peng et al., 2017; Xia et al., 2011; Zhao et al., 2014b), or display specific geochemical characteristics of adakites (Wang et al. 2006a) or sanukitoids (Tang et al., 2013; Xie et al., 2013). This has led to controversial interpretations of their magma sources, including partial melting of mantle wedge peridotites metasomatized

For Peer Review

by slab-derived fluids or sediments (An & Zhu et al., 2008; An et al., 2013; Wang et al., 2007; Xia et al., 2011; Xue et al., 2013), and interactions between subducted oceanic crust-derived melts and mantle wedge with or without crustal contamination (Wang et al., 2006a; Tang et al., 2013; Xie et al., 2013). However, the mafic to felsic varieties of the volcanic and plutonic rocks at Tulasu possess similar multi-element patterns (Figure 9), which might also suggest their origination from similar magma sources or from a common parental magma chamber (Tang et al., 2013; Xue et al. 2013; Zhao et al., 2014a).

The variations in Hf and Nd isotopic compositions have been proposed to be effective tools to decipher the magma source (Pearce, Kempton, & Gill, 2007; Vervoort et al., 2000). In general, the Hf and Nd isotope compositions of igneous rocks originated from recycled continental crust show low Lu/Hf and Sm/Nd ratios, together with negative $\varepsilon_{Hf}(t)$ and $\varepsilon_{Nd}(t)$ values, whereas those derived from depleted mantle have high Lu/Hf and Sm/Nd ratios, with positive $\varepsilon_{Hf}(t)$ and $\varepsilon_{Nd}(t)$ values (DePaolo, 1988; Kemp, Wormald, Whitehouse, & Price, 2005). As discussed in the previous section, fractional crystallization with insignificant crustal contamination has played an important role in the Axi-Tawuerbieke magma, whereas the Kexiaxi magmatism was dominantly by fractional crystallization with significant crust contamination and magma mixing processes.

In this study, zircon $\varepsilon_{Hf}(t)$ values of the volcanic and plutonic rocks from Axi-Tawuerbieke and Kexiaxi are uniform (mean = 5.0; n = 121), almost all falling between the depleted mantle evolution reference line and the chondrite uniform

http://mc.manuscriptcentral.com/gj

For Peer Review

reservoir line (Figure 10B). This indicates that these contemporaneous extrusive and intrusive rocks have a similar juvenile origin, and their parental magma were mainly derived from a depleted mantle with the involvement of supracrustal components. The whole-rock $\varepsilon_{Nd}(t)$ values (-4.2 to 4.6; n = 41) of these rocks are slightly more evolved than the depleted mantle. However, all the $\varepsilon_{Nd}(t)$ values are beyond the evolution continental crust reservoirs, plotting between the Bayingou ophiolites and the Yili crustal basement rocks, and hence also suggest a dominant depleted mantle source with variable contribution from the continental basement (Figure 10A). Besides, the majority of the samples show MgO concentration (Figure 8D) and $Mg^{\#}$ values (mean = 51; n = 105) higher than those of metabasaltic or eclogite experiment melts (Rapp & Watson, 1995), precluding their derivation from partial melting of the lower crust. Additionally, the highly evolved $\varepsilon_{Nd}(t)$ values of Kexiaxi quartz diorite and granodiorite samples (-4.2 to -2.2) compared to their positive zircon $\varepsilon_{Hf}(t)$ values of 1.6–6.9 might indicate decoupled Hf-Nd isotopic compositions of these rocks. The scenario of Hf–Nd isotopic decoupling was possibly caused by the higher solubility of Nd compared to Hf in the slab-derived components (Kessel, Schmidt, Ulmer, & Pettke, 2005; Polat & Münker, 2004), or through crustal contamination and magma mixing/mingling after zircon crystallization at shallow crust (Farmer and DePaolo, 1987; Vervoort et al., 2000).

Furthermore, the enrichment of LILEs relative to HFSEs, and scattered Nb/Yb (0.9–17.7) ratios of the volcanic and plutonic rocks (Figure 9) suggest that their mantle sources have been metasomatized by subduction slab-derived components

For Peer Review

(Elliott, 2003; Pearce, 2014). Their relatively high Th/Yb (0.8–11.4) and Th/Nb (0.8–1.3) ratios are consistent with metasomatism by slab-related sediments or sediment melts. This interpretation is additionally supported by the Ce/Pb vs. Th/La plot, in which most of the igneous rocks fall along the melt enrichment array (Figure 12E). In addition, the dominant samples possess low Ce/Ce* ratios, plotting in the field of arc rocks with the involvement of slab-derived melts (Hawkins & Ishizuka, 2009), distinct from the primitive arc rocks at Vanuatu, Palau and New Britain (Figure 12E).

Collectively, the coeval volcanic and plutonic rocks at the Tulasu district were most probably derived from a common depleted mantle source modified by slab-derived sedimentary melts. However, the evolution of the Axi-Tawuerbieke magma involving a dominant clinopyroxene-amphibole-plagioclase fractionation with insignificant crustal contamination. In contrast, the Kexiaxi magma involving differentiation through fractional crystallization, magma mixing/mingling, and significant continental crustal contamination. The different magmatic processes resulted in the variable geochemical and Sr-Nd isotopic compositions of the igneous rocks at Axi-Tawuerbieke and Kexiaxi. However, this does not preclude the fact that they have a similar origin.

6. 3 Volcanic-plutonic Connection of the Tulasu District

Devonian–Carboniferous volcanic and plutonic rocks at the Tulasu district host a series of epithermal gold and porphyry copper deposits (Figure 1C). While epithermal

For Peer Review

gold mineralization at the neighboring Axi and Tawuerbieke deposits appear to have been controlled by the 2.6- × 2.4-km Axi caldera (Figure 3A), occurring mainly in andesite, dacite and tuff of the Upper Andesite Member in the Dahalajunshan Volcanic Formation (DVF) as well as porphyritic granite intruding the DVF, the Kexiaxi porphyry copper prospect is characterized by stockwork Cu-Mo mineralization developed in a ~4.5 km^2 composite intrusion that emplaced into the Mesoproterozoic basement rocks (Figure 3B). However, the broader volcanic-plutonic connections and the mechanism operating in volcanic and plutonic realms and their associated mineralization at the Tulasu district are yet assessed.

The close spatial and temporal associations and comparable Sr-Nd-Hf isotope compositions of the Upper Andesite Member of the DVF and the hypabyssal porphyritic granite at Axi-Tawuerbieke indicate a direct volcanic-plutonic connection. It is noted that the porphyritic granite is compositionally much more evolved (SiO_2 = 72.68–77.15 wt.%) that the cogenetic andesitic rocks (Figure 8). Such a geochemical relationship seems to be inconsistent with the current popular 'crystal mush model' linking plutonic and volcanic rock suites (Bachmann & Bergantz, 2004), which highlighted that volcanic rocks are produced by extracting relatively evolved, rhyolitic magma melt from intermediate crystal mushes, whereas the residual mush pile crystalize incrementally to form the less evolved plutonic rocks (Bachmann & Bergantz, 2004; Bachmann et al., 2007). Even though the hypabyssal porphyritic granite is geochemically more evolved than the cogenetic andesitic rocks, their complementary relationship may indicate that the porphyritic granite represents the

For Peer Review

residual crystal mush after extraction of andesitic melt. This is also supported by their relatively steep REE patterns with no significant Eu anomalies (Figure 9F), indicating feldspar accumulation (Deering & Bachmann, 2010). Progressive fractional crystallization and crystal accumulation of the Axi caldera magma chamber resulted in the crystal mushes and the evolved melt (Bachmann et al., 2007). The crystal-rich characteristics of the andesitic rocks (Figure 4C) are indicative of inefficient separation of crystal from interstitial melt in the magma chamber, which conversely may have expelled volatile components accumulating at the top of the magma chamber (Parmigiani, Faroughi, Huber, Bachmann, & Su, 2016). It is likely that the most evolved felsic melts retained at the plutonic level, which effectively prevented their loss from volcanic eruption, but instead were crystallized to form the highly evolved granitoids. The model is similar to that presented by Cheng, Spandler, Chang, & Clarke (2018) for the middle Carboniferous cogenetic plutonic-volcanic sequence at the Herberton mineral field, northeastern Australia. Cheng et al. (2018) has indicated that the highly evolved intrusive rocks at Herberton represent the cumulate endmember of a felsic magmatic system, whereas the less evolved volcanic rocks represent the other endmember of the system.

Unlike the intra-caldera Axi-Tawuerbieke volcanic-plutonic complex in the center of the Tulasu district, the Kexiaxi composite pluton emplaced into Mesoproterozoic basement rocks along the margin of the district and thus provided no direct link with the volcanic sequence. However, the overlapping ages and similar magma sources from the Kexiaxi pluton and the Upper Andesite Member of the DVF

http://mc.manuscriptcentral.com/gj

For Peer Review

suggests an intimate comagmatic relationship. Specifically, the Kexiaxi pluton is overall compositionally equivalent to the cogenetic DVF rocks (Figs. 8 and 9). As discussed in the previous section, the observed geochemical gap of 56–64 wt.% SiO_2 for the Kexiaxi pluton might be caused by varying magma mixing/mingling and crustal contamination processes during magma evolution. Based on a combination of geochemical modeling, geochronology and textural observations, (Glazner et al., 2015) found that plutonic and volcanic rocks from convergent margin globally are also geochemical indistinguishable, and further suggested that the plutonic rocks are texturally modified samples of the same magmas for the volcanic rocks. In this scenario, magma fluxes may play a first-order role in igneous body evolution; that is large caldera-forming eruption formed by rapid emplacement rate (magma fluxes > 0.005 km^3/yr), whereas at lower magma fluxes producing small eruptions and plutons, and large volume plutons might be constructed incrementally over millions of years at a lower magma fluxes (Annen et al., 2015; Caricchi et al., 2014; Glazner et al., 2015).

6.4 Magma Fertility of Cogenetic Volcanic and Plutonic Rocks

Arc magma fertility studies have shown that the parental magma to form large porphyry Cu-Au deposits are necessarily water-rich, oxidized and have undergone moderate fractionation (Chiaradia, Ulianov, Kouzmanov, & Beate, 2012; Loucks, 2014; Richards, 2011; Richards, Spell, Rameh, Razique, & Fletcher, 2012; Sillitoe, 2010). A number of geochemical and petrological indicators have been formulated for

For Peer Review

application of unaltered intrusive rocks (Loucks, 2014). However, the intrusive rocks are commonly less outcropped in arc terranes, whereas the widely exposed volcanic sequences, particularly those that host important epithermal gold deposits, are thought to have close genetic links with potential porphyry Cu systems at depths (Buret et al., 2017; Hedenquist, Arribas, & Reynolds, 1998; Nadeau et al., 2016; Sillitoe, 2010) . Hence, these cogenetic volcanic sequences might also be used for fertility assessment (Behnsen, Spandler, Corral Calleja, Chang, & Dirks, 2016; Chen, Richards, Liang, Zou, Zhang, Huang, Ren & Wang, 2019).

Volcanic sequences of the DVF at Tulasu host important low- and high-sulfidation epithermal gold deposits (Figure 1C). They are relatively evolved, medium- to high-K calc-alkaline in compositions (Figs. 7 and 8). The presence of amphibole phenocrysts in the volcanic rocks (Figure 4D) indicate their parental magma was rich in magmatic water (≥ 4 wt.%) (Ridolfi, Renzulli, & Puerini, 2010; Rooney, Franceschi, & Hall, 2011), which is also supported by the depletion of middle REE (Figure 9) that caused by amphibole fractionation (Davidson, Turner, Handley, Macpherson & Dosseto, 2007). Considering the volcanic rocks have experienced variable hydrothermal alteration, we therefore used immobile Sc/V proxy to evaluate the magma fertility (Loucks, 2014). On the Sc/V vs. SiO_2 plot (Figure 13), both the Axi-Tawuerbieke volcanic samples and Kexiaxi plutonic samples show elevated V/Sc ratios, with some samples extended into the Cu-Au productive field (Loucks, 2014). In contrast, samples of the Tawuerbieke porphyritic granite plotted far away from the Cu-Au productive filed (Figure 13). Their significantly evolved

For Peer Review

geochemical signatures and low Cu concentration (1.9–22.3 ppm) conforms to a classification of being infertile for Cu mineralization. The observed scatter of V/Sc ratios in both samples might either reflect heterogeneity during volcanic processes (Cashman, Sparks, & Blundy, 2017) or caused by crustal contamination or magma mixing/mingling processes during emplacement. Hence, we suggest that the relatively hydrous and fertile nature of the magma that formed the DVF at Axi-Tawuerbieke area indicate a high potential for buried porphyry Cu deposits. This is further supported by the generally high Cu concentrations (5.4–174.2 ppm with an average of 45.9 ppm; Supplement TABLE DR2) in the volcanic rocks, the presence of native copper in basaltic andesite drill core (~162 m depths), as well as the monzonite porphyry enclaves in mineralized andesite at Tawuerbieke (Zhao et al., 2014b).

Coeval plutonic rocks at Kexiaxi represents the only porphyry Cu prospect at the Tulasu district. Abundant amphibole and biotite phenocrysts in all the four intrusive phases indicate high magmatic water contents of their parental magma. Although the Cu endowment of the Kexiaxi pluton is unknown yet, the high Cu concentration in fresh intrusive rocks (particularly the diorite porphyry possesses Cu concentration as high as 463 ppm; Supplement TABLE DR2), and relatively fertile nature of the parental magma might suggest a high prospecting potential. Fractional crystallization, magma mixing, and crustal contamination may have played important roles during Cu enrichment at Kexiaxi.

For Peer Review

7. CONCLUSIONS

(1) Calc-alkaline volcanism at Tulasu coincides with major plutonic activity at 347–367 Ma. The parental magma derives from a common depleted mantle source metasomatized by slab-derived melts, and their differentiation involved variable fractional crystallization, crustal contamination, and magma mixing.

(2) Highly evolved granites from the Axi caldera might be residuals left behind by extraction of erupted liquids/melts, whereas the Cu-bearing Kexiaxi pluton represent the intrusive equivalent of a common magma reservoir feeding the volcanic eruptions.

(3) The alteration-immobile geochemical indicator (e.g., V/Sc) for intrusive rocks may also be useful to assess the fertility of cogenetic volcanic rocks. Consequently, Kexiaxi and Tawuerbieke are important targets for future Cu-Au exploration at the Tulasu district.

For Peer Review

ACKNOWLEDGMENTS

This work was financially supported by the National Key R&D Program of China (2017YFC0601202), Natural Science Foundation of China (41602076 and U1303292), Fundamental Research Funds of the Central Universities (2652017212), the China Scholarship Council (Fellowship to XZ), and the Foreign Experts' Recruiting Program from the State Administration of Foreign Experts Affairs of China (G20190001238). We thank H.G., Wang for his help during field work, as well

as B., Feng, Z.X., Ding, M.N., Dai, H.Q., Xie and M., Liu for their laboratory assistance. RS acknowledges funding under NERC Grant 357 NE/ 1745 /1 “From arc magmas to ores (FAMOS): A mineral systems approach”. We thank the editors and anonymous reviewers for comments that greatly improved the presentation of the paper. This work is a contribution to IGCP project #662 under patronage of IUGS and UNESCO.

CONFLICT OF INTEREST

We declare there is no conflict of interest.

REFERENCES

An, F., Zhu, Y., Wei, S., & Lai, S. (2014). Geochronology and geochemistry of Shizishan sub-volcanic rocks in Jingxi-Yelmand gold deposit, Northwest Tianshan: Its petrogenesis and implications to tectonics and Au-mineralization. *Acta Petrologica Sinica, 30*(6), 1545-1557.

An, F., & Zhu, Y. F. (2008). Study on trace elements geochemistry and SHRIMP chronology of volcanic rocks in Tulasu basin, Northwest Tianshan. *Acta Petrologica Sinica, 24*(12), 2731-2748. (in Chinese with English abstract)

An, F., Zhu, Y., Wei, S., & Lai, S. (2013). An Early Devonian to Early Carboniferous volcanic arc in North Tianshan, NW China: Geochronological and geochemical evidence from volcanic rocks. *Journal of Asian Earth Sciences, 78*, 100-113.

For Peer Review

An, F., Zhu, Y., Wei, S., & Lai, S. (2017). The zircon U–Pb and Hf isotope constraints on the basement nature and Paleozoic evolution in northern margin of Yili Block, NW China. *Gondwana Research, 43*, 41-54.

Andersen, T. (2002). Correction of common lead in U–Pb analyses that do not report 204Pb. *Chemical geology, 192*(1-2), 59-79.

Annen, C. (2009). From plutons to magma chambers: Thermal constraints on the accumulation of eruptible silicic magma in the upper crust. *Earth and Planetary Science Letters, 284*(3-4), 409-416.

Annen, C., Blundy, J. D., Leuthold, J., & Sparks, R. S. J. (2015). Construction and evolution of igneous bodies: Towards an integrated perspective of crustal magmatism. *Lithos, 230*, 206-221.

Bachmann, O., & Bergantz, G. W. (2004). On the origin of crystal-poor rhyolites: extracted from batholithic crystal mushes. *Journal of Petrology, 45*(8), 1565-1582.

Bachmann, O., Miller, C. F., & De Silva, S. L. (2007). The volcanic–plutonic connection as a stage for understanding crustal magmatism. *Journal of Volcanology and Geothermal Research, 167*(1-4), 1-23.

Behnsen, H., Spandler, C., Corral Calleja, I., Chang, Z., & Dirks, P. H. (2016). Fertility of arc volcanic suites for Cu-Au mineralisation: a case study from NE Queensland, Australia.

Biske, Y. S., & Seltmann, R. (2010). Paleozoic Tian-Shan as a transitional region between the Rheic and Urals-Turkestan oceans. *Gondwana Research, 17*(2-3),

For Peer Review

602-613.

Black, L. P., Kamo, S. L., Allen, C. M., Aleinikoff, J. N., Davis, D. W., Korsch, R. J., & Foudoulis, C. (2003). TEMORA 1: a new zircon standard for Phanerozoic U–Pb geochronology. *Chemical geology, 200*(1-2), 155-170.

Blichert-Toft, J., & Albarède, F. (1997). The Lu-Hf isotope geochemistry of chondrites and the evolution of the mantle-crust system. *Earth and Planetary Science Letters, 148*(1-2), 243-258.

Buret, Y., Wotzlaw, J. F., Roozen, S., Guillong, M., von Quadt, A., & Heinrich, C. A. (2017). Zircon petrochronological evidence for a plutonic-volcanic connection in porphyry copper deposits. *Geology, 45*(7), 623-626.

Caricchi, L., Annen, C., Blundy, J., Simpson, G., & Pinel, V. (2014). Frequency and magnitude of volcanic eruptions controlled by magma injection and buoyancy. *Nature Geoscience, 7*(2), 126.

Cashman, K. V., Sparks, R. S. J., & Blundy, J. D. (2017). Vertically extensive and unstable magmatic systems: a unified view of igneous processes. *Science, 355*(6331), eaag3055.

Charvet, J., Shu, L., Laurent-Charvet, S., Wang, B., Faure, M., Cluzel, D., Chen, Y., & De Jong, K. (2011). Palaeozoic tectonic evolution of the Tianshan belt, NW China. *Science China Earth Sciences, 54*(2), 166-184.

Chen, X., Richards, J. P., Liang, H., Zou, Y., Zhang, J., Huang, W., Ren, L., & Wang, F. (2019). Contrasting arc magma fertilities in the Gangdese belt, Southern Tibet: Evidence from geochemical variations of Jurassic volcanic rocks. *Lithos, 324*,

For Peer Review

789-802.

Chen, Y. J., Pirajno, F., Wu, G., Qi, J. P., & Xiong, X. L. (2012). Epithermal deposits in north Xinjiang, NW China. *International Journal of Earth Sciences, 101*(4), 889-917.

Cheng, Y., Spandler, C., Chang, Z., & Clarke, G. (2018). Volcanic–plutonic connections and metal fertility of highly evolved magma systems: A case study from the Herberton Sn–W–Mo Mineral Field, Queensland, Australia. *Earth and Planetary Science Letters, 486*, 84-93.

Chiaradia, M., Ulianov, A., Kouzmanov, K., & Beate, B. (2012). Why large porphyry Cu deposits like high Sr/Y magmas?. *Scientific Reports, 2*, 685.

Cullen, J. T., Field, M. P., & Sherrell, R. M. (2001). Determination of trace elements in filtered suspended marine particulate material by sector field HR-ICP-MS. *Journal of Analytical Atomic Spectrometry, 16*(11), 1307-1312.

Davidson, J., Turner, S., Handley, H., Macpherson, C., & Dosseto, A. (2007). Amphibole “sponge” in arc crust?. *Geology, 35*(9), 787-790.

Deering, C. D., & Bachmann, O. (2010). Trace element indicators of crystal accumulation in silicic igneous rocks. *Earth and Planetary Science Letters, 297*(1-2), 324-331.

Deering, C. D., Keller, B., Schoene, B., Bachmann, O., Beane, R., & Ovtcharova, M. (2016). Zircon record of the plutonic-volcanic connection and protracted rhyolite melt evolution. *Geology, 44*(4), 267-270.

DePAOLO, D. J. (1981). Trace element and isotopic effects of combined wallrock

For Peer Review

assimilation and fractional crystallization. *Earth and planetary science letters, 53*(2), 189-202.

DePaolo, D. J. (1988). Age dependence of the composition of continental crust: evidence from Nd isotopic variations in granitic rocks. *Earth and Planetary Science Letters, 90*(3), 263-271.

Dong, L., Wan, B., Deng, C., Cai, K., & Xiao, W. (2018). An Early Permian epithermal gold system in the Tulasu Basin in North Xinjiang, NW China: constraints from in situ oxygen-sulfur isotopes and geochronology. *Journal of Asian Earth Sciences, 153*, 412-424.

Elhlou, S., Belousova, E., Griffin, W. L., Pearson, N. J., & O'Reilly, S. Y. (2006). Trace element and isotopic composition of GJ-red zircon standard by laser ablation. *Geochimica et Cosmochimica Acta Supplement, 70*, A158-A158.

Elliott, T. (2003). Tracers of the slab. *Geophysical Monograph-American Geophysical Union, 138*, 23-46.

Fan, W. M., Guo, F., Wang, Y. J., & Zhang, M. (2004). Late Mesozoic volcanism in the northern Huaiyang tectono-magmatic belt, central China: partial melts from a lithospheric mantle with subducted continental crust relicts beneath the Dabie orogen?. *Chemical Geology, 209*(1-2), 27-48.

Farmer, G. L., & DePaolo, D. J. (1987). Nd and Sr isotope study of hydrothermally altered granite at San Manuel, Arizona; implications for element migration paths during the formation of porphyry copper ore deposits. *Economic Geology, 82*(5), 1142-1151.

For Peer Review

FGTXBGMR (First Geological Team of Xinjiang Bureau of Geology and Mineral Resources), 1990, Geological Map 1: 50000, Peizhongzhan and Qie'erge Sheet (L–44–140–A, B).

Gao, J., Klemd, R., Qian, Q., Zhang, X., Li, J., Jiang, T., & Yang, Y. (2011). The collision between the Yili and Tarim blocks of the Southwestern Altaids: geochemical and age constraints of a leucogranite dike crosscutting the HP–LT metamorphic belt in the Chinese Tianshan Orogen. *Tectonophysics, 499*(1-4), 118-131.

Gao, J., Li, M., Xiao, X., Tang, Y., & He, G. (1998). Paleozoic tectonic evolution of the Tianshan Orogen, northwestern China. *Tectonophysics, 287*(1-4), 213-231.

Gao, J., Long, L., Klemd, R., Qian, Q., Liu, D., Xiong, X., Su, W., Liu, W., Wang, Y., & Yang, F. (2009). Tectonic evolution of the South Tianshan orogen and adjacent regions, NW China: geochemical and age constraints of granitoid rocks. *International Journal of Earth Sciences, 98*(6), 1221-1238.

Gao, J., Wang, X. S., Klemd, R., Jiang, T., Qian, Q., Mu, L. X., & Ma, Y. Z. (2015). Record of assembly and breakup of Rodinia in the Southwestern Altaids: evidence from Neoproterozoic magmatism in the Chinese Western Tianshan Orogen. *Journal of Asian Earth Sciences, 113*, 173-193.

Ge, R., Zhu, W., Wu, H., Zheng, B., Zhu, X., & He, J. (2012). The Paleozoic northern margin of the Tarim Craton: passive or active?. *Lithos, 142*, 1-15.

Glazner, A. F., Coleman, D. S., & Mills, R. D. (2015). The volcanic-plutonic connection. In Physical geology of shallow magmatic systems (pp. 61-82).

For Peer Review

Springer, Cham.

Griffin, W. L., Pearson, N. J., Belousova, E., Jackson, S. V., Van Achterbergh, E., O'Reilly, S. Y., & Shee, S. R. (2000). The Hf isotope composition of cratonic mantle: LAM-MC-ICPMS analysis of zircon megacrysts in kimberlites. *Geochimica et Cosmochimica Acta, 64*(1), 133-147.

Griffin, W. L., Wang, X., Jackson, S. E., Pearson, N. J., O'Reilly, S. Y., Xu, X., & Zhou, X. (2002). Zircon chemistry and magma mixing, SE China: in-situ analysis of Hf isotopes, Tonglu and Pingtan igneous complexes. *Lithos, 61*(3-4), 237-269.

Han, B. F., He, G. Q., Wang, X. C., & Guo, Z. J. (2011). Late Carboniferous collision between the Tarim and Kazakhstan–Yili terranes in the western segment of the South Tian Shan Orogen, Central Asia, and implications for the Northern Xinjiang, western China. *Earth-Science Reviews, 109*(3-4), 74-93.

Han, B. F., Guo, Z. J., Zhang, Z. C., Zhang, L., Chen, J. F., & Song, B. (2010). Age, geochemistry, and tectonic implications of a late Paleozoic stitching pluton in the North Tian Shan suture zone, western China. *Bulletin, 122*(3-4), 627-640.

Han, Y., & Zhao, G. (2018). Final amalgamation of the Tianshan and Junggar orogenic collage in the southwestern Central Asian Orogenic Belt: constraints on the closure of the Paleo-Asian Ocean. *Earth-Science Reviews, 186*, 129-152.

Hastie, A. R., Kerr, A. C., Pearce, J. A., & Mitchell, S. F. (2007). Classification of altered volcanic island arc rocks using immobile trace elements: development of the Th–Co discrimination diagram. *Journal of petrology, 48*(12), 2341-2357.

For Peer Review

Hawkins, J. W., & Ishizuka, O. (2009). Petrologic evolution of Palau, a nascent island arc. *Island Arc, 18*(4), 599-641.

He, J., Zhang, Y., Wang, Y., Qian, X., & Sun, L. (2018). Late Paleozoic post-collisional setting of the North Tianshan, NW China: New insights from geochronology, geochemistry and Sr–Nd isotopic compositions of the Permian Nileke volcanic rocks. *Lithos, 318*, 314-325.

Hedenquist, J. W., Arribas, A., & Reynolds, T. J. (1998). Evolution of an intrusion-centered hydrothermal system; Far Southeast-Lepanto porphyry and epithermal Cu-Au deposits, Philippines. *Economic Geology, 93*(4), 373-404.

Hibbard, M. J. (1981). The magma mixing origin of mantled feldspars. *Contributions to Mineralogy and Petrology, 76*(2), 158-170.

Hollings, P., Cooke, D., & Clark, A. (2005). Regional geochemistry of Tertiary igneous rocks in central Chile: Implications for the geodynamic environment of giant porphyry copper and epithermal gold mineralization. *Economic Geology, 100*(5), 887-904.

Hora, J. M., Singer, B. S., Wörner, G., Beard, B. L., Jicha, B. R., & Johnson, C. M. (2009). Shallow and deep crustal control on differentiation of calc-alkaline and tholeiitic magma. *Earth and Planetary Science Letters, 285*(1-2), 75-86.

Huang, Z., Long, X., Kröner, A., Yuan, C., Wang, Q., Sun, M., Zhao, G., & Wang, Y. (2013). Geochemistry, zircon U–Pb ages and Lu–Hf isotopes of early Paleozoic plutons in the northwestern Chinese Tianshan: petrogenesis and geological implications. *Lithos, 182*, 48-66.

For Peer Review

Keller, C. B., Schoene, B., Barboni, M., Samperton, K. M., & Husson, J. M. (2015a). Volcanic–plutonic parity and the differentiation of the continental crust. *Nature, 523*(7560), 301.

Kemp, A. I. S., Hawkesworth, C. J., Foster, G. L., Paterson, B. A., Woodhead, J. D., Hergt, J. M., Gray, C. M., & Whitehouse, M. J. (2007). Magmatic and crustal differentiation history of granitic rocks from Hf-O isotopes in zircon. *Science, 315*(5814), 980-983.

Kemp, A. I. S., Wormald, R. J., Whitehouse, M. J., & Price, R. C. (2005). Hf isotopes in zircon reveal contrasting sources and crystallization histories for alkaline to peralkaline granites of Temora, southeastern Australia. *Geology, 33*(10), 797-800.

Kessel, R., Schmidt, M. W., Ulmer, P., & Pettke, T. (2005). Trace element signature of subduction-zone fluids, melts and supercritical liquids at 120–180 km depth. *Nature, 437*(7059), 724.

Klemd, R., Bröcker, M., Hacker, B. R., Gao, J., Gans, P., & Wemmer, K. (2005). New age constraints on the metamorphic evolution of the high-pressure/low-temperature belt in the western Tianshan Mountains, NW China. *The Journal of Geology, 113*(2), 157-168.

Klemd, R., John, T., Scherer, E. E., Rondenay, S., & Gao, J. (2011). Changes in dip of subducted slabs at depth: petrological and geochronological evidence from HP–UHP rocks (Tianshan, NW-China). *Earth and Planetary Science Letters, 310*(1-2), 9-20.

For Peer Review

Large, R. R., Allen, R. L., Blake, M. D., & Herrmann, W. (2001). Hydrothermal alteration and volatile element halos for the Rosebery K lens volcanic-hosted massive sulfide deposit, western Tasmania. *Economic Geology, 96*(5), 1055-1072.

Le Maitre, R., Bateman, P., Dudek, A., Keller, J., Lameyre, J., Le Bas, M., Sabine, P., Schmid, R., Sorensen, H., & Streckeisen, A., (1989). A classification of igneous rocks and glossary of terms. Recommendations of the IUGS Subcommission on the Systematics of Igneous rocks: London: Blackwell Scientific Publications.

Li, Q. L., Lin, W., Su, W., Li, X. H., Shi, Y. H., Liu, Y., & Tang, G. Q. (2011). SIMS U–Pb rutile age of low-temperature eclogites from southwestern Chinese Tianshan, NW China. *Lithos, 122*(1-2), 76-86.

Liu, H., Wang, B., Shu, L., Jahn, B. M., & Lizuka, Y. (2014). Detrital zircon ages of Proterozoic meta-sedimentary rocks and Paleozoic sedimentary cover of the northern Yili Block: Implications for the tectonics of microcontinents in the Central Asian Orogenic Belt. *Precambrian Research, 252*, 209-222.

Long, L., Gao, J., Klemd, R., Beier, C., Qian, Q., Zhang, X., ... & Jiang, T. (2011). Geochemical and geochronological studies of granitoid rocks from the Western Tianshan Orogen: implications for continental growth in the southwestern Central Asian Orogenic Belt. *Lithos, 126*(3-4), 321-340.

Loucks, R. R. (2014). Distinctive composition of copper-ore-forming arcmagmas. *Australian Journal of Earth Sciences, 61*(1), 5-16.

Ludwig, K. R. (2003). User's manual for IsoPlot 3.0. A Geochronological Toolkit for

For Peer Review

Microsoft Excel, 71.

Lundstrom, C. C., & Glazner, A. F. (2016). Silicic magmatism and the volcanic–plutonic connection. *Elements, 12*(2), 91-96.

Nadeau, O., Stix, J., & Williams-Jones, A. E. (2016). Links between arc volcanoes and porphyry-epithermal ore deposits. *Geology, 44*(1), 11-14.

Parmigiani, A., Faroughi, S., Huber, C., Bachmann, O., & Su, Y. (2016). Bubble accumulation and its role in the evolution of magma reservoirs in the upper crust. *Nature, 532*(7600), 492.

Pearce, J. A., Kempton, P. D., & Gill, J. B. (2007). Hf–Nd evidence for the origin and distribution of mantle domains in the SW Pacific. *Earth and Planetary Science Letters, 260*(1-2), 98-114.

Pearce, J. A. (2014). Immobile element fingerprinting of ophiolites. *Elements, 10*(2), 101-108.

Peng, Y. W., Gu, X. X., Cheng, W. B., Zhao, X. B., Wang, G. N., Lu, L. T., & Han, J. M. (2018). Metallogenesis of the late Palaeozoic Axi–Tawuerbieke Au–Pb–Zn district in the Tulasu Basin, western Tianshan, China: constraints from geological characteristics and isotope geochemistry. *Geological Journal, 53*(6), 3030-3050.

Peng, Y. W., Gu, X. X., Lv, P. R., Zhang, Y. M., Cheng, W. B., & Wang, X. L. (2017). Genesis and tectonic setting of the Late Devonian Tawuerbieke gold deposit in the Tulasu ore cluster, western Tianshan, Xinjiang, China. *International Geology Review, 59*(10), 1344-1368.

For Peer Review

Polat, A., & Münker, C. (2004). Hf–Nd isotope evidence for contemporaneous subduction processes in the source of late Archean arc lavas from the Superior Province, Canada. *Chemical Geology, 213*(4), 403-429.

Qian, Q., Gao, J., Klemd, R., He, G., Song, B., Liu, D., & Xu, R. (2009). Early Paleozoic tectonic evolution of the Chinese South Tianshan Orogen: constraints from SHRIMP zircon U–Pb geochronology and geochemistry of basaltic and dioritic rocks from Xiate, NW China. *International Journal of Earth Sciences, 98*(3), 551-569.

Rapp, R. P., & Watson, E. B. (1995). Dehydration melting of metabasalt at 8–32 kbar: implications for continental growth and crust-mantle recycling. *Journal of Petrology, 36*(4), 891-931.

Richards, J. P. (2011). Magmatic to hydrothermal metal fluxes in convergent and collided margins. *Ore Geology Reviews, 40*(1), 1-26.

Richards, J. P., Spell, T., Rameh, E., Razique, A., & Fletcher, T. (2012). High Sr/Y magmas reflect arc maturity, high magmatic water content, and porphyry Cu±Mo±Au potential: Examples from the Tethyan arcs of central and eastern Iran and western Pakistan. *Economic Geology, 107*(2), 295-332.

Ridolfi, F., Renzulli, A., & Puerini, M. (2010). Stability and chemical equilibrium of amphibole in calc-alkaline magmas: an overview, new thermobarometric formulations and application to subduction-related volcanoes. *Contributions to Mineralogy and Petrology, 160*(1), 45-66.

Rollinson, H. (1993). Using geochemical data: Evaluation, presentation, interpretation

For Peer Review

(pp. 1–352). Harlow, England: Longman.

Rooney, T. O., Franceschi, P., & Hall, C. M. (2011). Water-saturated magmas in the Panama Canal region: a precursor to adakite-like magma generation?. *Contributions to Mineralogy and Petrology, 161*(3), 373-388.

Rui, Z., Goldfarb, R. J., Qiu, Y., Zhou, T., Chen, R., Pirajno, F., & Yun, G. (2002). Paleozoic–early Mesozoic gold deposits of the Xinjiang Autonomous Region, northwestern China. *Mineralium Deposita, 37*(3-4), 393-418.

Scherer, E., Münker, C., & Mezger, K. (2001). Calibration of the lutetium-hafnium clock. *Science, 293*(5530), 683-687.

Şengör, A. M. C., Natal'In, B. A., & Burtman, V. S. (1993). Evolution of the Altaid tectonic collage and Palaeozoic crustal growth in Eurasia. *Nature, 364*(6435), 299-307.

Sha, D. M., Wu, R. S., Tian, C. L., Yang, S., & Jia, B. (1999). Late Paleozoic Axi paleocaldera in west Tianshan Mountains and its ore-controlling significance. *Geological Review, 45*, 1088-1094. (in Chinese with English abstract)

Shu, L., Wang, B., Zhu, W., Guo, Z., Charvet, J., & Zhang, Y. (2011). Timing of initiation of extension in the Tianshan, based on structural, geochemical and geochronological analyses of bimodal volcanism and olistostrome in the Bogda Shan (NW China). *International Journal of Earth Sciences, 100*(7), 1647-1663.

Sillitoe, R. H. (1973). The tops and bottoms of porphyry copper deposits. *Economic Geology, 68*(6), 799-815.

Sillitoe, R. H. (2010). Porphyry copper systems. Economic geology, 105(1), 3-41.

For Peer Review

Su, W., Cai, K., Sun, M., Wan, B., Wang, X., Bao, Z., & Xiao, W. (2018). Carboniferous volcanic rocks associated with back-arc extension in the western Chinese Tianshan, NW China: Insight from temporal-spatial character, petrogenesis and tectonic significance. *Lithos, 310*, 241-254.

Su, W., Gao, J., Klemd, R., Li, J. L., Zhang, X., Li, X. H., Chen, N.S., & Zhang, L. (2010). U–Pb zircon geochronology of Tianshan eclogites in NW China: implication for the collision between the Yili and Tarim blocks of the southwestern Altaids. *European Journal of Mineralogy, 22*(4), 473-478.

Sun, S. S., & McDonough, W. F. (1989). Chemical and isotopic systematics of oceanic basalts: implications for mantle composition and processes. *Geological Society, London, Special Publications, 42*(1), 313-345.

Tang, G.J., Wang, Q., Zhao, Z.H., Wyman, D.A., Chen, H.H., Jia, X.H., & Jiang, Z.Q. (2009). LA-ICP-MS zircon U–Pb geochronology, element geochemistry and petrogenesis of the andesites in the eastern Taerbieke gold deposit of the western Tianshan region. *Acta Petrologica Sinica, 25*(6), 1341-1352. (in Chinese with English abstract)

Tang, G. J., Wang, Q., Wyman, D. A., Sun, M., Zhao, Z. H., & Jiang, Z. Q. (2013). Petrogenesis of gold-mineralized magmatic rocks of the Taerbieke area, northwestern Tianshan (western China): Constraints from geochronology, geochemistry and Sr–Nd–Pb–Hf isotopic compositions. *Journal of Asian Earth Sciences, 74*, 113-128.

Vervoort, J. D., Patchett, P. J., Albarède, F., Blichert-Toft, J., Rudnick, R., &

For Peer Review

Downes, H. (2000). Hf–Nd isotopic evolution of the lower crust. *Earth and Planetary Science Letters, 181*(1-2), 115-129.

Wang, B., Cluzel, D., Shu, L., Faure, M., Charvet, J., Chen, Y., Meffre, S., & De Jong, K. (2009). Evolution of calc-alkaline to alkaline magmatism through Carboniferous convergence to Permian transcurrent tectonics, western Chinese Tianshan. *International Journal of Earth Sciences, 98*(6), 1275-1298.

Wang, B., Faure, M., Shu, L., Cluzel, D., Charvet, J., De Jong, K., & Chen, Y. (2008). Paleozoic tectonic evolution of the Yili Block, western Chinese Tianshan. *Bulletin de la Société Géologique de France, 179*(5), 483-490.

Wang, B., Jahn, B. M., Shu, L., Li, K., Chung, S. L., & Liu, D. (2012). Middle-Late Ordovician arc-type plutonism in the NW Chinese Tianshan: Implication for the accretion of the Kazakhstan continent in Central Asia. *Journal of Asian Earth Sciences, 49*, 40-53.

Wang, B., Liu, H., Shu, L., Jahn, B. M., Chung, S. L., Zhai, Y., & Liu, D. (2014a). Early Neoproterozoic crustal evolution in northern Yili Block: insights from migmatite, orthogneiss and leucogranite of the Wenquan metamorphic complex in the NW Chinese Tianshan. *Precambrian Research, 242*, 58-81.

Wang, B., Liu, H., Shu, L., Jahn, B. M., Chung, S. L., Zhai, Y., & Liu, D. (2014b). Early Neoproterozoic crustal evolution in northern Yili Block: insights from migmatite, orthogneiss and leucogranite of the Wenquan metamorphic complex in the NW Chinese Tianshan. *Precambrian Research, 242*, 58-81.

Wang, B., Shu, L. S., Cluzel, D., Faure, M., & Charvet, J. (2007). Geochemical

For Peer Review

constraints on Carboniferous volcanic rocks of the Yili Block (Xinjiang, NW China): implication for the tectonic evolution of Western Tianshan. *Journal of Asian Earth Sciences, 29*(1), 148-159.

Wang, Q., Zhao, Z. H., Xu, J. F., Wyman, D. A., Xiong, X. L., Zi, F., & Bai, Z. H. (2006). Carboniferous adakite-high-Mg andesite-Nb-enriched basaltic rock suites in the Northern Tianshan area: Implications for Phanerozoic crustal growth in the Central Asia Orogenic Belt and Cu-Au mineralization. *Acta Petrologica Sinica, 22*(1), 11-30. (in Chinese with English abstract)

Wang, X. S., Gao, J., Klemd, R., Jiang, T., Li, J. L., Zhang, X., & Xue, S. C. (2017). The Central Tianshan Block: A microcontinent with a Neoarchean-Paleoproterozoic basement in the southwestern Central Asian orogenic belt. *Precambrian Research, 295*, 130-150.

Williams, I. S. (1998). U-Th-Pb geochronology by ion microprobe: Reviews in Economic Geology, v. 7.

Williams, N. C., & Davidson, G. J. (2004). Possible submarine advanced argillic alteration at the Basin Lake prospect, Western Tasmania, Australia. *Economic Geology, 99*(5), 987-1002.

Winchester, J. A., & Floyd, P. A. (1976). Geochemical magma type discrimination: application to altered and metamorphosed basic igneous rocks. *Earth and Planetary Science Letters, 28*(3), 459-469.

Windley, B. F., Alexeiev, D., Xiao, W., Kröner, A., & Badarch, G. (2007). Tectonic models for accretion of the Central Asian Orogenic Belt. *Journal of the*

For Peer Review

Geological Society, 164(1), 31-47.

Woodhead, J. D., & Hergt, J. M. (2005). A preliminary appraisal of seven natural zircon reference materials for in situ Hf isotope determination. *Geostandards and Geoanalytical Research, 29*(2), 183-195.

Xia, H., Chen, G. W., Liu, Q., & Luo, Y. (2011). Geochemical characteristics of the Dahalajunshan formation volcanic rocks in the Tulasu Basin of Western Tianshan and its tectonic implications. *Geotectonica et Metallogenia, 35*(3), 429-438. (in Chinese with English abstract)

Xia, L.Q., Xia, Z.C., Xu, X.Y., Li, X.M., Ma, Z.P., & Wang, L.S. (2007), Magmatism of the Tianshan. (pp. 1-359). Geological Publishing House, Beijing. (in Chinese).

Xiao, L., Nick, H., Graham, B., Fu, Minlu., Wang, F., & Pirajno, F. (2005). The Jinxi–Yelmand high-sulfidation epithermal gold deposit, Western Tianshan, Xinjiang Province, PR China. *Ore Geology Reviews, 26*(1-2), 17-37.

Xiao, W., & Santosh, M. (2014). The western Central Asian Orogenic Belt: a window to accretionary orogenesis and continental growth. *Gondwana Research, 25*(4), 1429-1444.

Xiao, W., Windley, B. F., Allen, M. B., & Han, C. (2013). Paleozoic multiple accretionary and collisional tectonics of the Chinese Tianshan orogenic collage. *Gondwana Research, 23*(4), 1316-1341.

Xiao, X.C., Tang, Y.Q., Feng, Y.M., Zhu, B.Z., Li, J., & Zhao, M. (1992). The Tectonic Evolution of North Xinjiang and Its Adjacent Regions. (pp. 1-190). Geological Publishing House, Beijing. (in Chinese).

For Peer Review

XBGMR (Xinjiang Bureau of Geology and Mineral Resources). (1993). Regional Geology of Xinjiang Uygur Autonomous Region. Geological Publishing House, Beijing. (in Chinese).

Xie, H. J., Wu, G., Zhu, M. T., Zhong, W., Liu, J., Mei, M., & Wang, Y. W. (2013). Qiarbahete Sanukitoids and adakitic rocks in NW Tianshan: age and geochemical constraints on their petrogenesis and tectonic settings. *International Geology Review, 55*(15), 1941-1958.

Xing, H., Zhao, X. B., Zhang, Z. C., Ye, J. C., & Feng, B. (2016). Early Paleozoic geological environment of metallogeny in Bavinbuluk region, western Tien Shan: igneous rocks and their dating, elementary and isotopic constraints. *Acta Petrol. Sin, 32*, 1770-1794. (In Chinese with English abstract)

Xue, C. J., Wang, H. G., Zhao, X. B., & Chen, L. Y. (2013). Kexiaxi cluster of small intrusions in the Tulasu gold mineralization district, Western Tianshan, Xinjiang, and its copper exploration prospect. *Earth Science Frontiers, 20*(6), 180-194. (in Chinese with English abstract).

Xu, X. Y., Li, X. M., Ma, Z. P., Xia, L. Q., Xia, Z. C., & Peng, S. X. (2006). LA-ICPMS zircon U-Pb dating of gabbro from the Bayingou ophiolite in the northern Tianshan Mountains. *Acta Geologica Sinica, 80*(8), 1168-1176. (in Chinese with English abstract).

Xu, X. Y., Wang, H. L., Li, P., Chen, J. L., Ma, Z. P., Zhu, T., ... & Dong, Y. P. (2013). Geochemistry and geochronology of Paleozoic intrusions in the Nalati (Narati) area in western Tianshan, Xinjiang, China: implications for Paleozoic

For Peer Review

tectonic evolution. *Journal of Asian Earth Sciences, 72*, 33-62.

Yan, L., He, Z., Beier, C., & Klemd, R. (2018). Geochemical constraints on the link between volcanism and plutonism at the Yunshan caldera complex, SE China. *Contributions to Mineralogy and Petrology, 173*(1), 4.

Yang, F., Mao, J., Bierlein, F. P., Pirajno, F., Zhao, C., Ye, H., & Liu, F. (2009). A review of the geological characteristics and geodynamic mechanisms of Late Paleozoic epithermal gold deposits in North Xinjiang, China. *Ore Geology Reviews, 35*(2), 217-234.

Yu, X., Wang, Z., Zhou, X., Xiao, W., & Yang, X. (2016). Zircon U–Pb geochronology and Sr–Nd isotopes of volcanic rocks from the Dahalajunshan Formation: implications for Late Devonian–Middle Carboniferous tectonic evolution of the Chinese Western Tianshan. *International Journal of Earth Sciences, 105*(5), 1637-1661.

Yuan, H. L., Gao, S., Dai, M. N., Zong, C. L., Günther, D., Fontaine, G. H., ... & Diwu, C. (2008). Simultaneous determinations of U–Pb age, Hf isotopes and trace element compositions of zircon by excimer laser-ablation quadrupole and multiple-collector ICP-MS. *Chemical Geology, 247*(1-2), 100-118.

Zhai, W., Sun, X., Sun, W., Su, L., He, X., & Wu, Y. (2009). Geology, geochemistry, and genesis of Axi: a Paleozoic low-sulfidation type epithermal gold deposit in Xinjiang, China. *Ore Geology Reviews, 36*(4), 265-281.

Zhai, W., Sun, X., Gao, J., He, X., Liang, J., Miao, L., & Wu, Y. (2006). SHRIMP dating of zircons from volcanic host rocks of Dahalajunshan Formation in Axi

For Peer Review

gold deposit, Xinjiang, China, and its geological implications. *Acta Petrologica Sinica, 22*(5), 1399-1404.

Zhao, X., Xue, C., Chi, G., Wang, H., & Qi, T. (2014a). Epithermal Au and polymetallic mineralization in the Tulasu Basin, western Tianshan, NW China: Potential for the discovery of porphyry CuAu deposits. *Ore Geology Reviews, 60*, 76-96.

Zhao, X., Xue, C., Symons, D. T., Zhang, Z., & Wang, H. (2014b). Microgranular enclaves in island-arc andesites: A possible link between known epithermal Au and potential porphyry Cu–Au deposits in the Tulasu ore cluster, western Tianshan, Xinjiang, China. *Journal of Asian Earth Sciences, 85*, 210-223.

Zhao, Z., Zhang, Z., Santosh, M., Huang, H., Cheng, Z., & Ye, J. (2015). Early Paleozoic magmatic record from the northern margin of the Tarim Craton: Further insights on the evolution of the Central Asian Orogenic Belt. *Gondwana Research, 28*(1), 328-347.

Zhong, L., Wang, B., Alexeiev, D. V., Cao, Y., Biske, Y. S., Liu, H., Zhai, Y., & Xing, L. (2017). Paleozoic multi-stage accretionary evolution of the SW Chinese Tianshan: New constraints from plutonic complex in the Nalati Range. *Gondwana Research, 45*, 254-274.

Zhu, Y., Guo, X., Song, B., Zhang, L., & Gu, L. (2009). Petrology, Sr–Nd–Hf isotopic geochemistry and zircon chronology of the Late Palaeozoic volcanic rocks in the southwestern Tianshan Mountains, Xinjiang, NW China. *Journal of the Geological Society, 166*(6), 1085-1099.

For Peer Review

Zonenshaĭn, L. P., Kuz′min, M. I., & Natapov, L. M. (1990). Geology of the USSR: a plate-tectonic synthesis, American Geophysical Union.

FIGURE CAPTIONS

FIGURE 1 (A) Tectonic outline of the Central Asian Orogenic Belt, modified after Sengör, Natal'In, & Burtman (1993), showing the position of the Chinese western Tianshan. (B) Schematic geological map of the Chinese western Tianshan, modified after Gao et al. (2009) and Han et al., (2011), showing the location of the Tulasu ore district within the northern margin of the Yili Block. (C) Geological map of the Tulasu ore district showing the distribution of Devono-Carboniferous igneous rocks and associated epithermal Au-Pb-Zn and Cu porphyry deposits (Zhai et al., 2009). Age data sources: Zhai et al. (2006); Tang et al. (2009); An et al. (2014); An et al. (2013); Zhao et al. (2014a); Zhao et al., (2014b); Peng et al. (2017)

FIGURE 2 Stratigraphic sections of the Upper Paleozoic sequences of the Tulasu ore district, showing the spatial and temporal framework of the Dahalajunshan Volcanic Formation (DVF), and gold-hosting rock suits of the Axi, Jingxi-Yelmend and Tawuerbieke deposits

FIGURE 3 (A) Geological map of the Axi-Tawuerbieke gold deposit (modified after Zhao et al., 2014a). (B) Geological map of the Kexiaxi porphyry copper deposit (modified after Xue et al., 2013)

For Peer Review

FIGURE 4 Field photos and photomicrographs of the late Paleozoic volcanic and plutonic rocks of the Tulasu ore district. (A) Round-shaped monzonite porphyry enclave (MPE) hosted in the DVF andesite from western Tawuerbieke deposit area. (B) Early Carboniferous porphyritic granite at Tawuerbieke. (C) Late Devonian andesite with abundant phenocrysts of plagioclase at Tawuerbieke. (D) Porphyritic texture of the andesite (# AX-2; Axi deposit) with amphibole and plagioclase phenocrysts under cross-polarized light. (E) Porphyritic texture of andesite (# TWE-20; Tawuerbieke) with plagioclase and clinopyroxene phenocrysts under cross-polarized light. (F) Porphyritic granite (# TWE-35; Tawuerbieke) showing plagioclase, K-feldspar and quartz phenocrysts under cross-polarized light. (G) Contact relationship between diorite porphyry and quartz diorite at Kexiaxi; (H) Mafic microgranular enclaves (MMEs) hosted in granodiorite at Kexiaxi. The MMEs show rounded to ovoid in shape and have interfaces with the host granodiorite. Inset showing xenocrysts of plagioclase and quartz in the MMEs. (I) Equigranular gabbroic diorite (# KXX-23; Kexiaxi) with abundant plagioclase, clinopyroxene, and amphibole, with less biotite and Fe-Ti oxides under cross-polarized light. (J) Quartz diorite (# KXX-33; Kexiaxi) has a coarse-grained equigranular texture with abundant plagioclase, quartz, amphibole and biotite under cross-polarized light. (K) Equigranular granodiorite (# KXX-11; Kexiaxi) with abundant plagioclase, K-feldspar, quartz and biotite under cross-polarized light. (L) Diorite porphyry (# KXX-14; Kexiaxi) showing plagioclase and amphibole phenocrysts under

For Peer Review

cross-polarized light. Abbreviations: Note: Pl–plagioclase; Kfs–K-feldspar; Amp–amphibole; Qtz–quartz; Bt–biotite; Cpx–clinopyroxene

FIGURE 5 Representative cathodoluminescence photographs of zircon grains from volcanic and plutonic rocks of the Tulasu ore district. Solid and dashed circles indicate the locations of U–Pb zircon dating and in situ Lu-Hf analyses. See Table1 for individual analyses and corresponding ratios and ages. Zircon U-Pb SHRIMP ages for samples TWE-20 and TWE-8 from Tawuerbieke were reported in Zhao et al. (2014a), and for samples KXX-23, KXX-11, KXX-33, and KXX-14 from Kexiaxi were reported by Xue et al. (2013)

FIGURE 6 (A) SHRIMP U-Pb zircon Concordia plot for the porphyritic granite (# TWE-35) from Tawuerbieke. (B) LA-ICP-MS U-Pb zircon Concordia plot for the andesite (# AX-2) from Axi. MSWD–mean square of weighted deviates

FIGURE 7 Geochemical classification and discrimination diagrams for volcanic and plutonic rocks from the Tulasu ore district. (A) Total alkali versus silica (TAS) diagram (Le Maitre et al., 1989). (B) Nb/Y versus $Zr/TiO_2 \times 0.0001$ plot (Winchester and Floyd, 1976). (C) Th–Co diagram (Hastie et al., 2007). Full datasets see Supplement TABLE DR2

For Peer Review

1293

1294 **FIGURE 8** Variations of selected major and trace element concentrations versus SiO_2
1295 for volcanic and plutonic rocks from the Tulasu ore district. Full datasets see
1296 Supplement TABLE DR2

1297

1298 **FIGURE 9** Primitive mantle-normalized trace element and chondrite-normalized rare
1299 earth element (REE) patterns for volcanic and plutonic rocks from the Tulasu ore
1300 district. Normalizing values after (Sun & McDonough, 1989). Full datasets see
1301 Supplement TABLE DR2

1302

1303 **FIGURE 10** (A) Whole-rock Sr-Nd isotopic compositions for volcanic and plutonic
1304 rocks of the Tulasu ore district. (B) Epsilon Hf*(t)* versus U-Pb age for zircon grains
1305 from the volcanic and plutonic rocks of the Tulasu district. Sources for whole-rock
1306 Sr-Nd isotope data: Neoproterozoic basement of the Yili Block (Wang et al., 2014a)
1307 and Bayingou ophiolite (Xia et al. 2007). Sources for zircon Hf isotope data: volcanic
1308 rocks (An et al., 2017; Tang et al., 2013) and plutonic rocks (Tang et al., 2013).
1309 Abbreviations: DM = depleted mantle; LCC = lower continental crust; UCC = upper
1310 continental crust

1311

1312 **FIGURE 11** (A) Alteration Box plot (Williams & Davidson, 2004), showing all

For Peer Review

volcanic and plutonic samples of the Tulasu ore district. Dashed arrow indicates the trend from least altered towards the pyrophyllite alteration zones. The Ishikawa Alteration Index (AI) = $100\times[K_2O+MgO]/[K_2O+MgO+Na_2O+CaO]$, and the Advanced Argillic Alteration Index (AAAI) = $100\times Si_2O/[Si_2O+10\times MgO+10\times Na_2O+10\times CaO]$. Full datasets see Supplement TABLE DR2. (B-D) Variation diagrams of loss on ignition (LOI) with $^{87}Sr/^{86}Sr_{(i)}$, $^{143}Nd/^{144}Nd_{(i)}$ and $\varepsilon_{Nd}(t)$ for volcanic and plutonic rock samples of the Tulasu district

FIGURE 12 Variation diagrams with geochemical trends to discriminate the petrogenetic processes for the volcanic and plutonic rocks of the Tulasu ore district. (A) Yb vs. Tb/Yb (Fan et al., 2004), (B) SiO_2 vs. Dy/Yb (Davidson et al., 2007), (C) SiO_2 vs. $\varepsilon_{Nd}(t)$, (D) $^{147}Sm/^{144}Nd$ vs. $^{143}Nd/^{144}Nd$, (E) Th/La vs. Ce/Pb and (F) Ce/Ce* vs. Th plots (Hawkins & Ishizuka, 2009)

FIGURE 13 Whole-rock V/Sc vs. SiO_2 magma fertility discrimination plot (Loucks, 2014)

TABLE CAPTIONS

TABLE 1 Description of the studied volcanic (DVF) and plutonic rock samples of the Tulasu ore district

For Peer Review

TABLE 2 Summary of zircon U-Pb ages and Hf isotopes of the volcanic (DVF) and plutonic rocks of the Tulasu ore district

SUPPLEMENT TABLE CAPTIONS

TABLE DR1 Zircon SHRIMP and LA-ICPMS U–Pb data of the late Paleozoic volcanic and plutonic rocks, Tulasu ore district

TABLE DR 2 Compilation of whole-rock major (wt.%) and trace element (ppm) compositions of the late Paleozoic volcanic and plutonic rocks, Tulasu ore district

TABLE DR3 Whole-rock Sr-Nd isotopic ratios of the late Paleozoic volcanic and plutonic rocks, Tulasu ore district

TABLE DR4 In-situ zircon Hf isotope data of the late Paleozoic volcanic and plutonic rocks, Tulasu ore district

For Peer Review

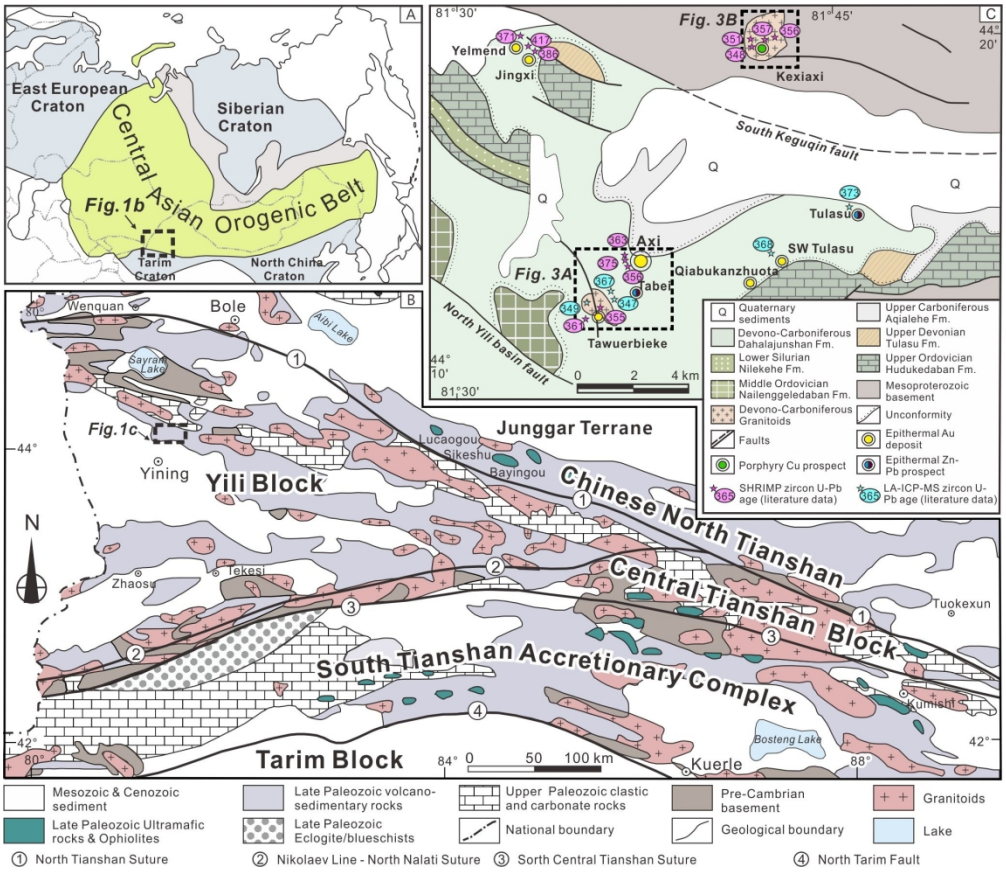

FIGURE 1 (A) Tectonic outline of the Central Asian Orogenic Belt, modified after Sengör, Natal'In, & Burtman (1993), showing the position of the Chinese western Tianshan. (B) Schematic geological map of the Chinese western Tianshan, modified after Gao et al. (2009) and Han et al., (2011), showing the location of the Tulasu ore district within the northern margin of the Yili Block. (C) Geological map of the Tulasu ore district showing the distribution of Devono-Carboniferous igneous rocks and associated epithermal Au-Pb-Zn and Cu porphyry deposits (Zhai et al., 2009). Age data sources: Zhai et al. (2006); Tang et al. (2009); An et al. (2014); An et al. (2013); Zhao et al. (2014a); Zhao et al., (2014b); Peng et al. (2017)

174x150mm (300 x 300 DPI)

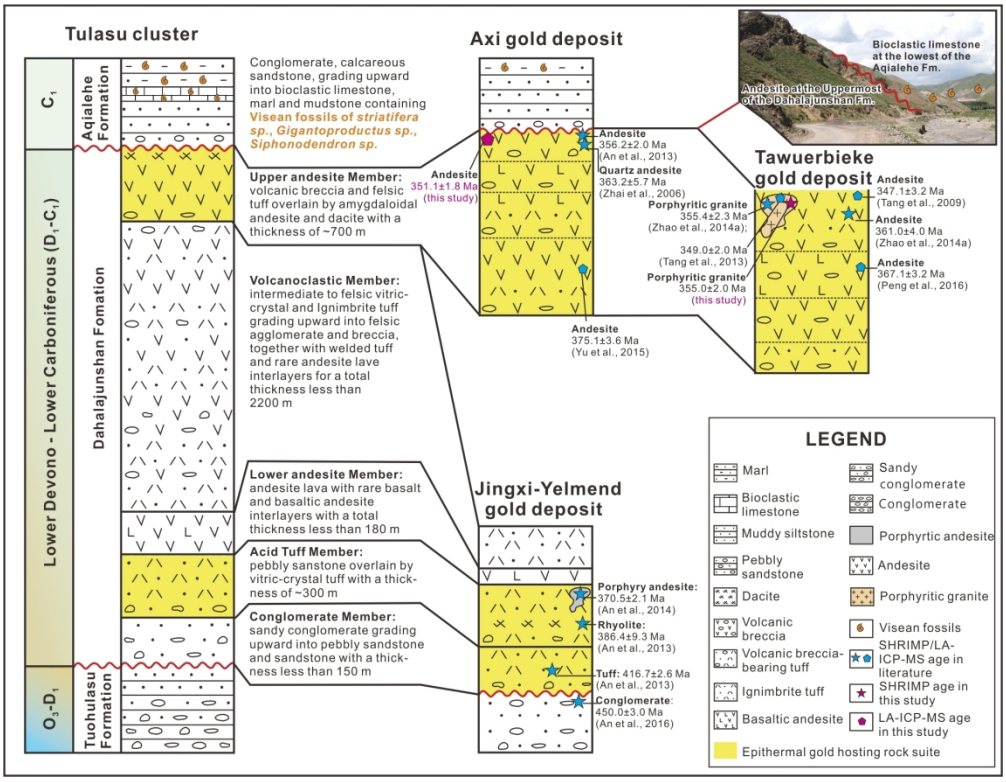

Figure 2.Stratigraphic sections of the Upper Paleozoic sequences of the Tulasu ore district, showing the spatial and temporal framework of the Dahalajunshan Volcanic Formation (DVF), and gold-hosting rock suits of the Axi, Jingxi-Yelmend and Tawuerbieke deposits.

175x135mm (300 x 300 DPI)

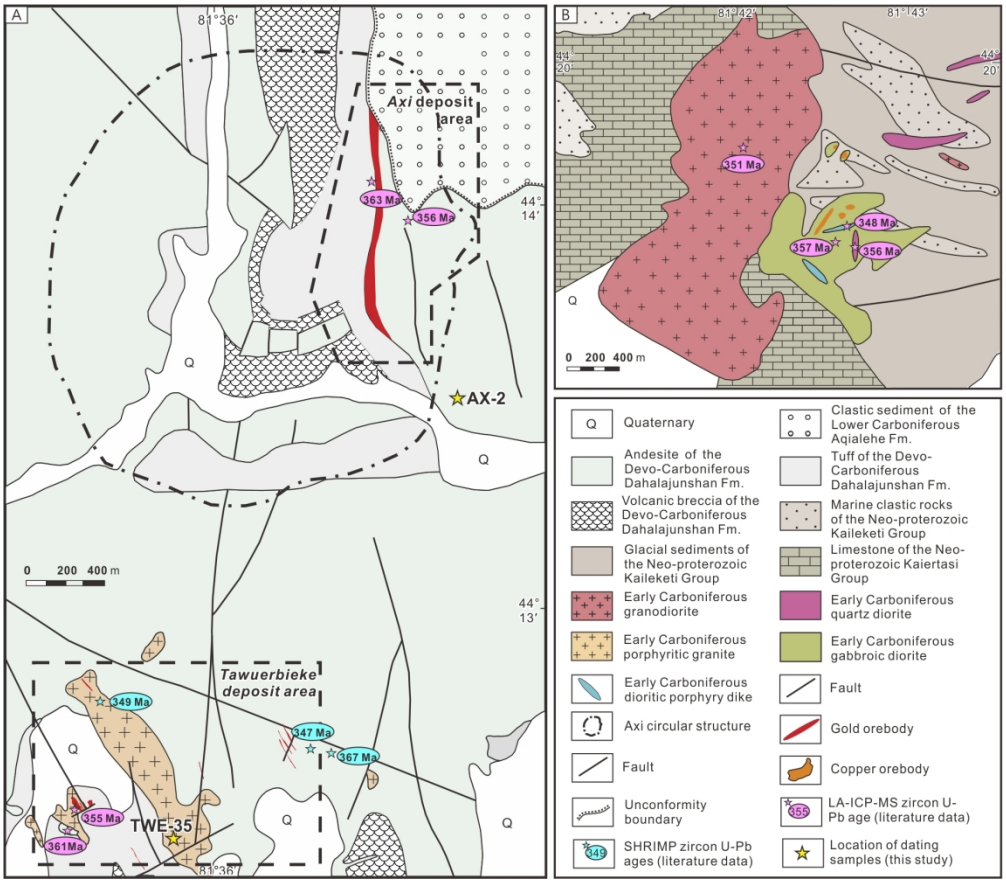

Figure 3. (A) Geological map of the Axi-Tawuerbieke gold deposit (modified after Zhao et al., 2014a). (B) Geological map of the Kexiaxi porphyry copper deposit (modified after Xue et al., 2013).

168x147mm (300 x 300 DPI)

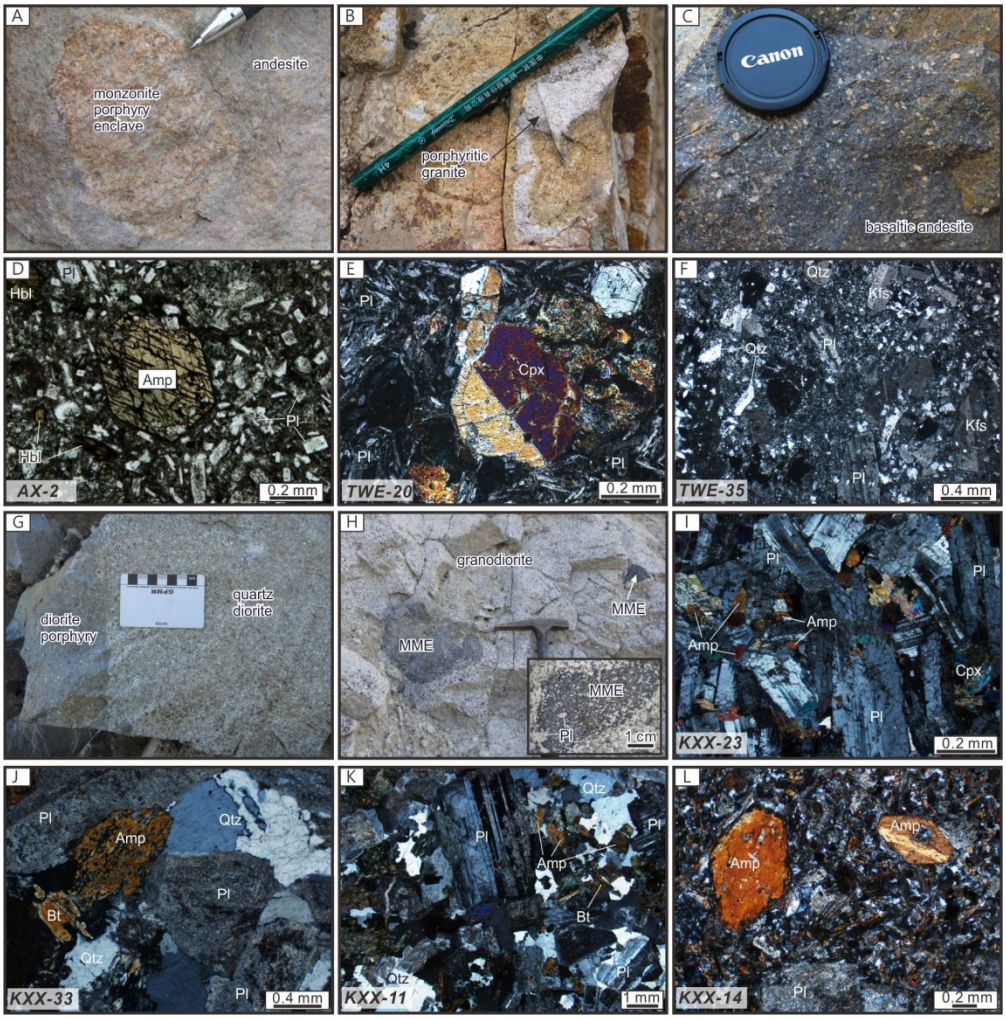

FIGURE 4 Field photos and photomicrographs of the late Paleozoic volcanic and plutonic rocks of the Tulasu ore district. (A) Round-shaped monzonite porphyry enclave (MPE) hosted in the DVF andesite from western Tawuerbieke deposit area. (B) Early Carboniferous porphyritic granite at Tawuerbieke. (C) Late Devonian andesite with abundant phenocrysts of plagioclase at Tawuerbieke. (D) Porphyritic texture of the andesite (# AX-2; Axi deposit) with amphibole and plagioclase phenocrysts under cross-polarized light. (E) Porphyritic texture of andesite (# TWE-20; Tawuerbieke) with plagioclase and clinopyroxene phenocrysts under cross-polarized light. (F) Porphyritic granite (# TWE-35; Tawuerbieke) showing plagioclase, K-feldspar and quartz phenocrysts under cross-polarized light. (G) Contact relationship between diorite porphyry and quartz diorite at Kexiaxi; (H) Mafic microgranular enclaves (MMEs) hosted in granodiorite at Kexiaxi. The MMEs show rounded to ovoid in shape and have interfaces with the host granodiorite. Inset showing xenocrysts of plagioclase and quartz in the MMEs. (I) Equigranular gabbroic diorite (# KXX-23; Kexiaxi) with abundant plagioclase, clinopyroxene, and amphibole, with less biotite and Fe-Ti oxides under cross-polarized light. (J) Quartz diorite (# KXX-33; Kexiaxi) has a coarse-grained equigranular texture with abundant plagioclase, quartz, amphibole and biotite under cross-polarized light. (K) Equigranular granodiorite (# KXX-11; Kexiaxi) with abundant plagioclase, K-feldspar, quartz and biotite under cross-polarized light. (L) Diorite porphyry (# KXX-14; Kexiaxi) showing plagioclase and amphibole phenocrysts under cross-polarized light. Abbreviations: Note: Pl–plagioclase; Kfs–K-feldspar; Amp–amphibole; Qtz–quartz; Bt–biotite; Cpx–clinopyroxene

148x149mm (300 x 300 DPI)

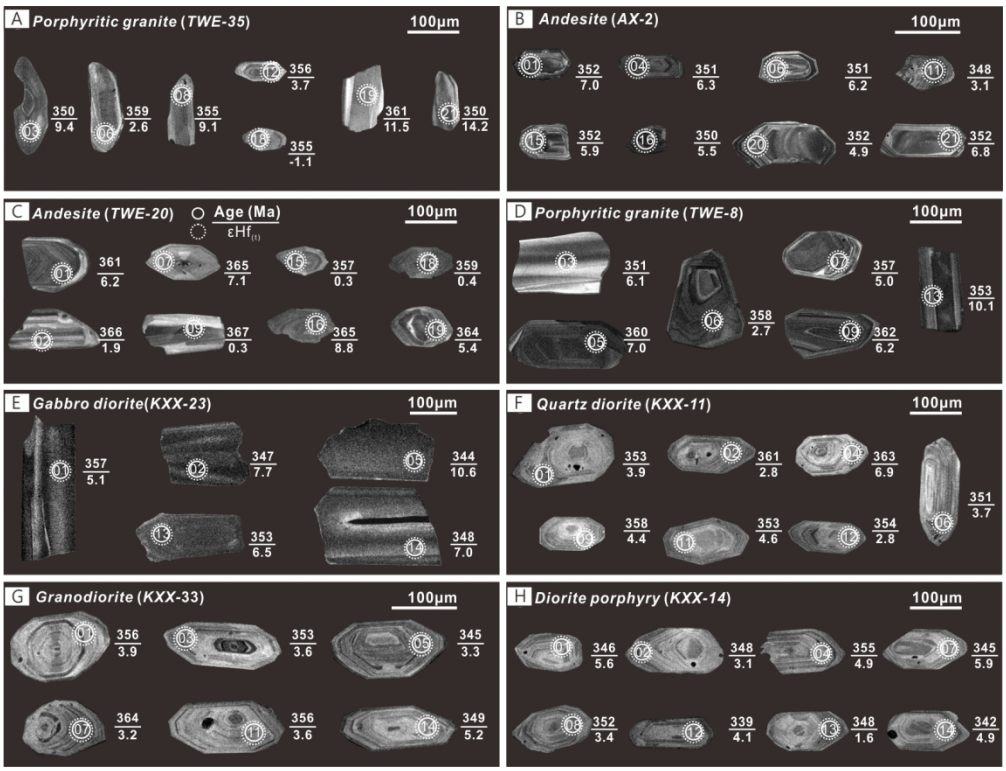

Figure 5.Representative cathodoluminescence photographs of zircon grains from volcanic and plutonic rocks of the Tulasu ore district. Solid and dashed circles indicate the locations of U–Pb zircon dating and in situ Lu-Hf analyses. See Table1 for individual analyses and corresponding ratios and ages. Zircon U-Pb SHRIMP ages for samples TWE-20 and TWE-8 from Tawuerbieke were reported in Zhao et al. (2014a), and for samples KXX-23, KXX-11, KXX-33, and KXX-14 from Kexiaxi were reported by Xue et al. (2013).

144x109mm (300 x 300 DPI)

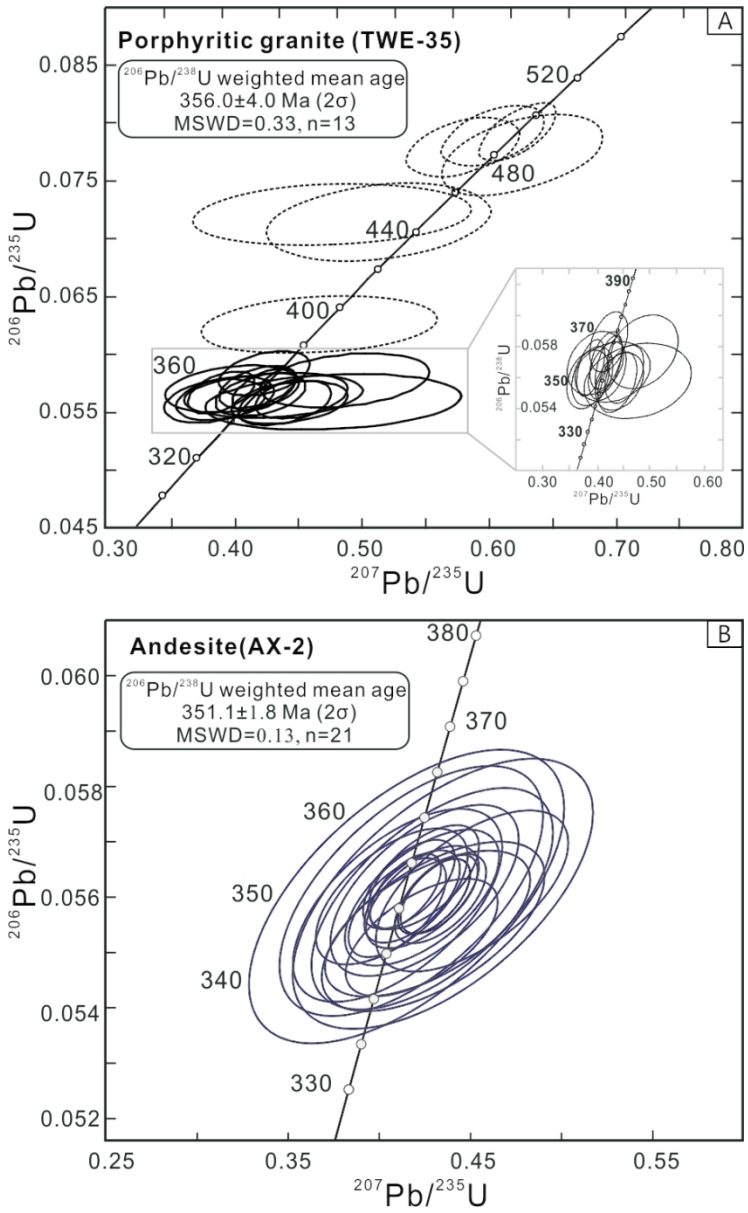

Figure 6. (A) SHRIMP U-Pb zircon Concordia plot for the porphyritic granite (# TWE-35) from Tawuerbieke. (B) LA-ICP-MS U-Pb zircon Concordia plot for the andesite (# AX-2) from Axi. MSWD–mean square of weighted deviates.

78x127mm (300 x 300 DPI)

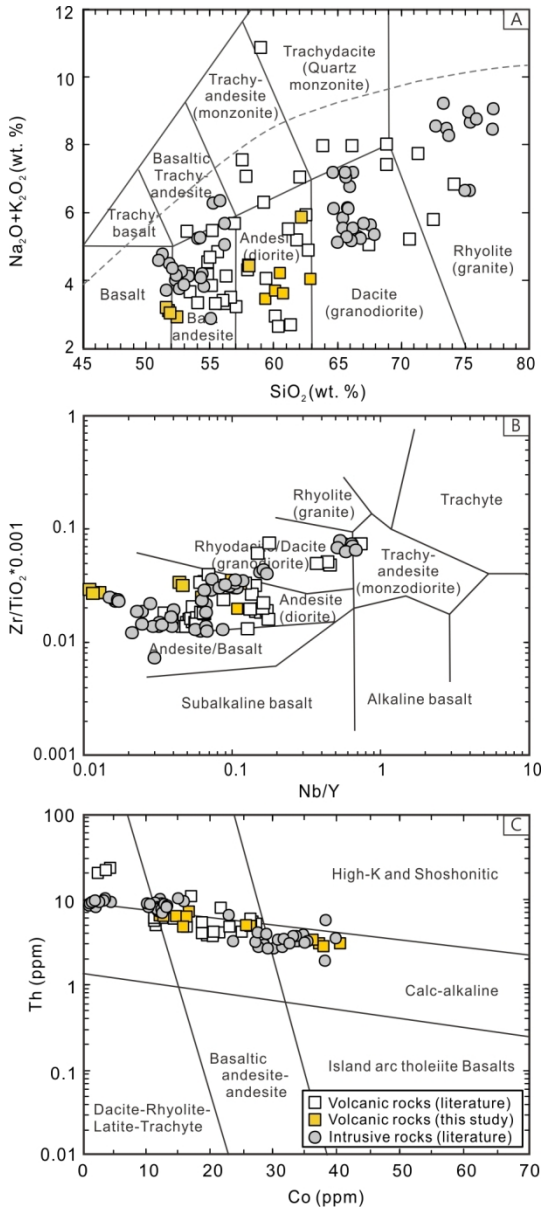

Figure 7. Geochemical classification and discrimination diagrams for volcanic and plutonic rocks from the Tulasu ore district. (A) Total alkali versus silica (TAS) diagram (Le Maitre et al., 1989). (B) Nb/Y versus Zr/TiO2×0.0001 plot (Winchester and Floyd, 1976). (C) Th–Co diagram (Hastie et al., 2007). Full datasets see Supplement Table DR2.

77x173mm (300 x 300 DPI)

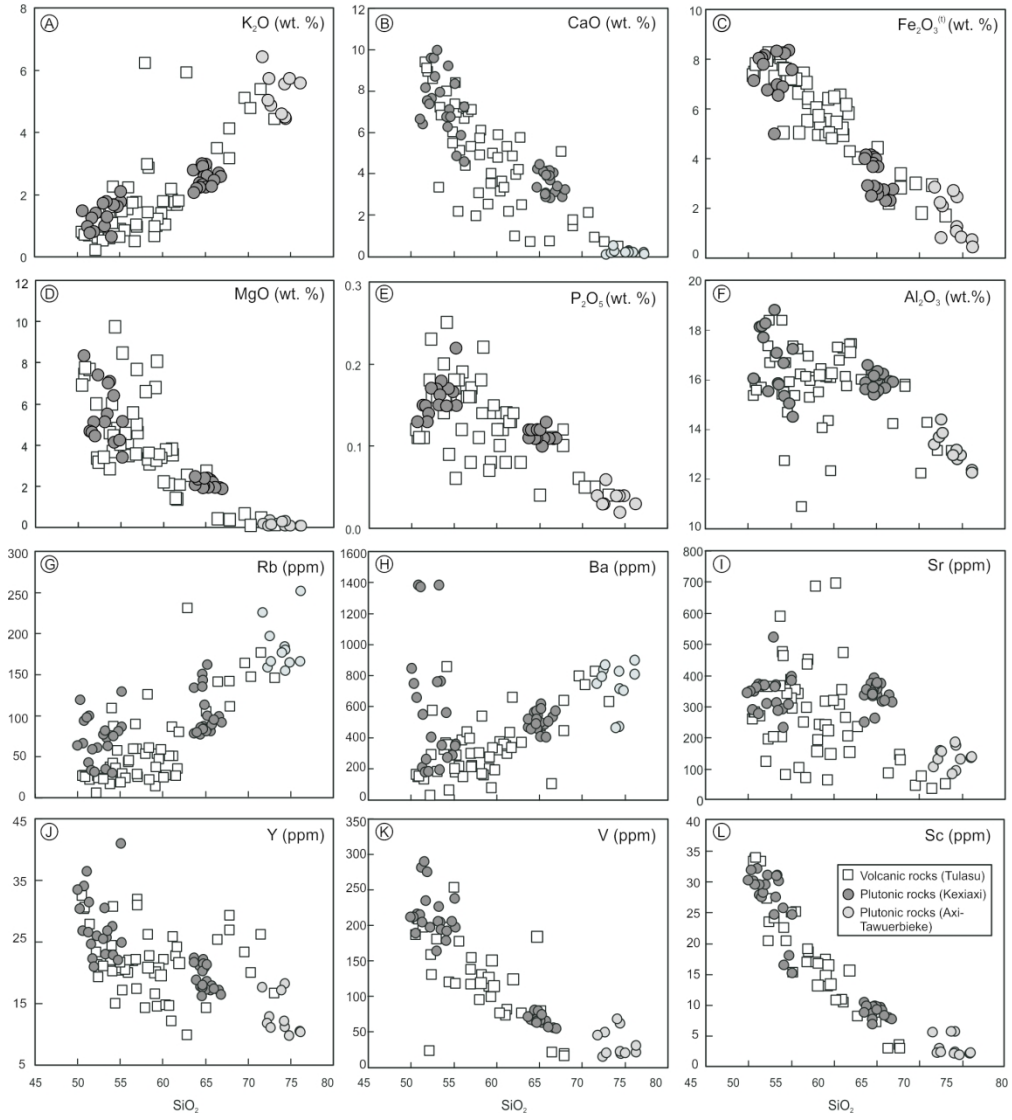

Figure 8. Variations of selected major and trace element concentrations versus SiO2 for volcanic and plutonic rocks from the Tulasu ore district. Full datasets see Supplement Table DR2.

175x194mm (300 x 300 DPI)

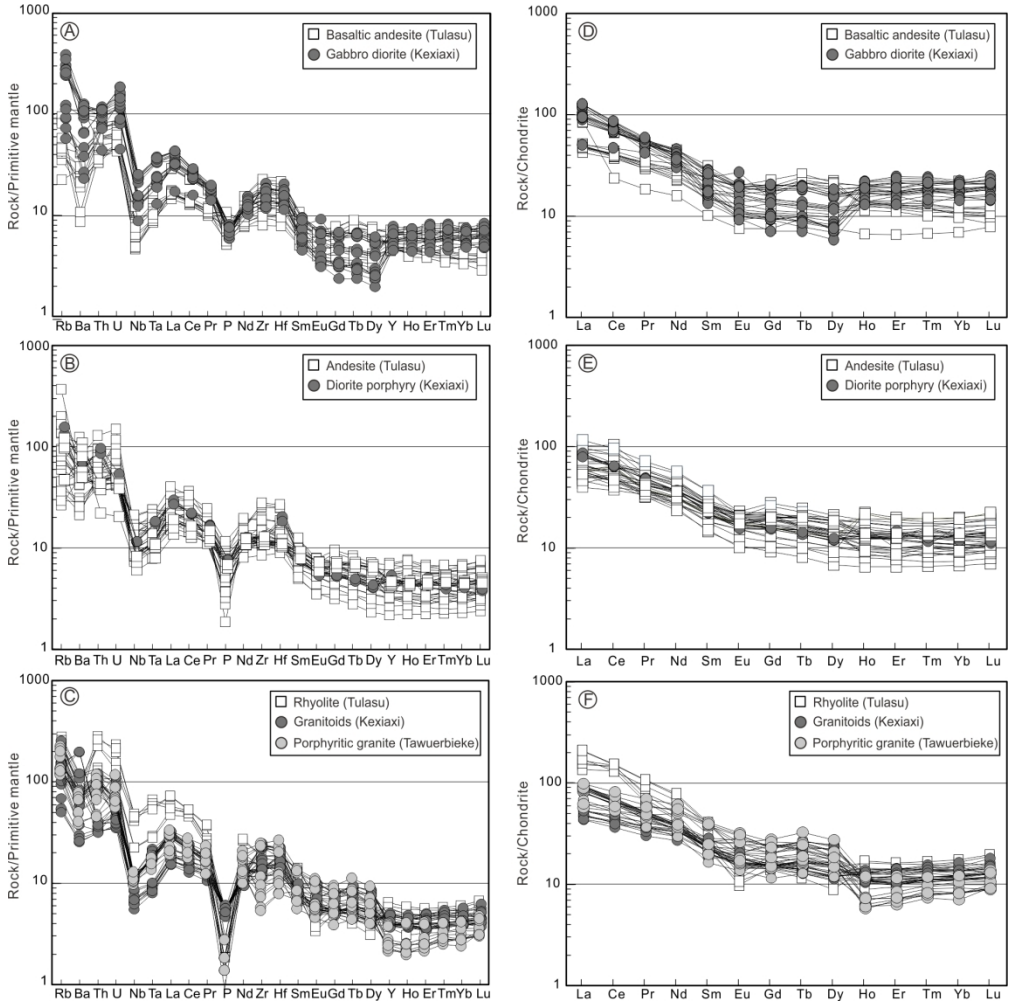

Figure 9. Primitive mantle-normalized trace element and chondrite-normalized rare earth element (REE) patterns for volcanic and plutonic rocks from the Tulasu ore district. Normalizing values after (Sun and McDonough, 1989). Full datasets see Supplement Table DR2.

167x167mm (300 x 300 DPI)

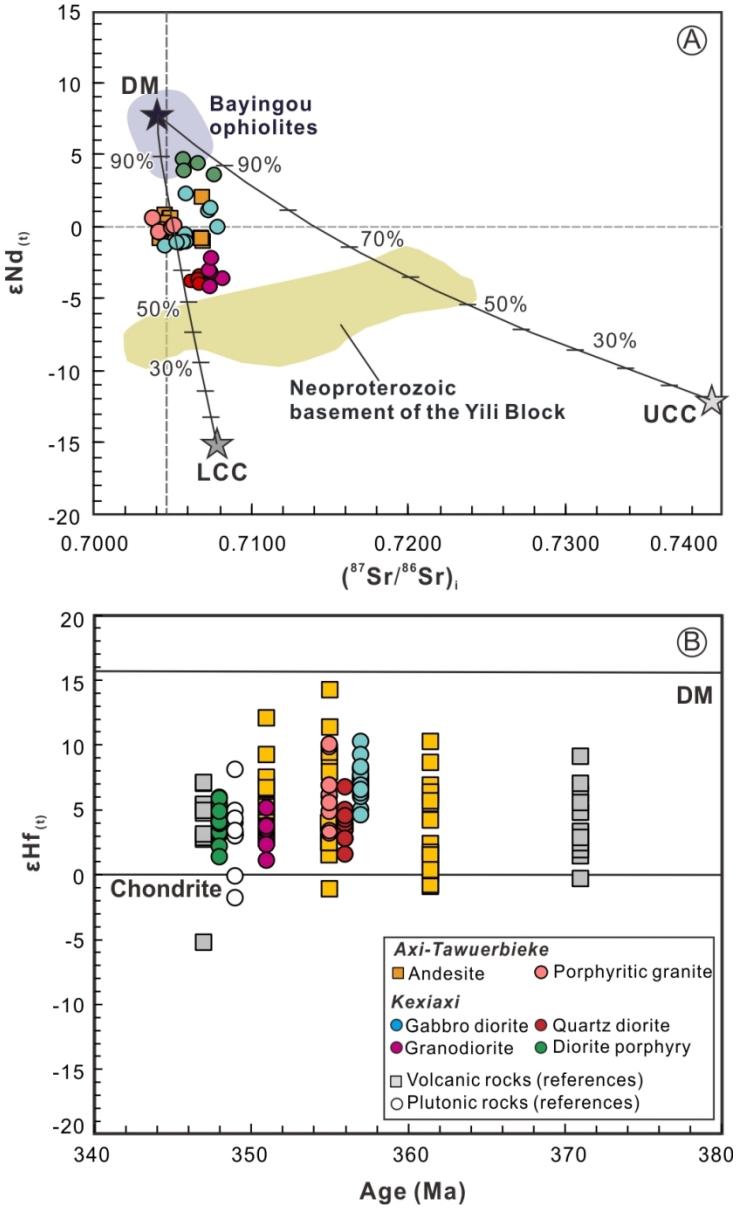

Figure 10. (A) Whole-rock Sr-Nd isotopic compositions for volcanic and plutonic rocks of the Tulasu ore district. (B) Epsilon Hf(t) versus U-Pb age for zircon grains from the volcanic and plutonic rocks of the Tulasu district. Sources for whole-rock Sr-Nd isotope data: Neoproterozoic basement of the Yili Block (Wang et al., 2014a) and Bayingou ophiolite (Xia et al. 2007). Sources for zircon Hf isotope data: volcanic rocks (An et al., 2017; Tang et al., 2013) and plutonic rocks (Tang et al., 2013). Abbreviations: DM = depleted mantle; LCC = lower continental crust; UCC = upper continental crust.

87x143mm (300 x 300 DPI)

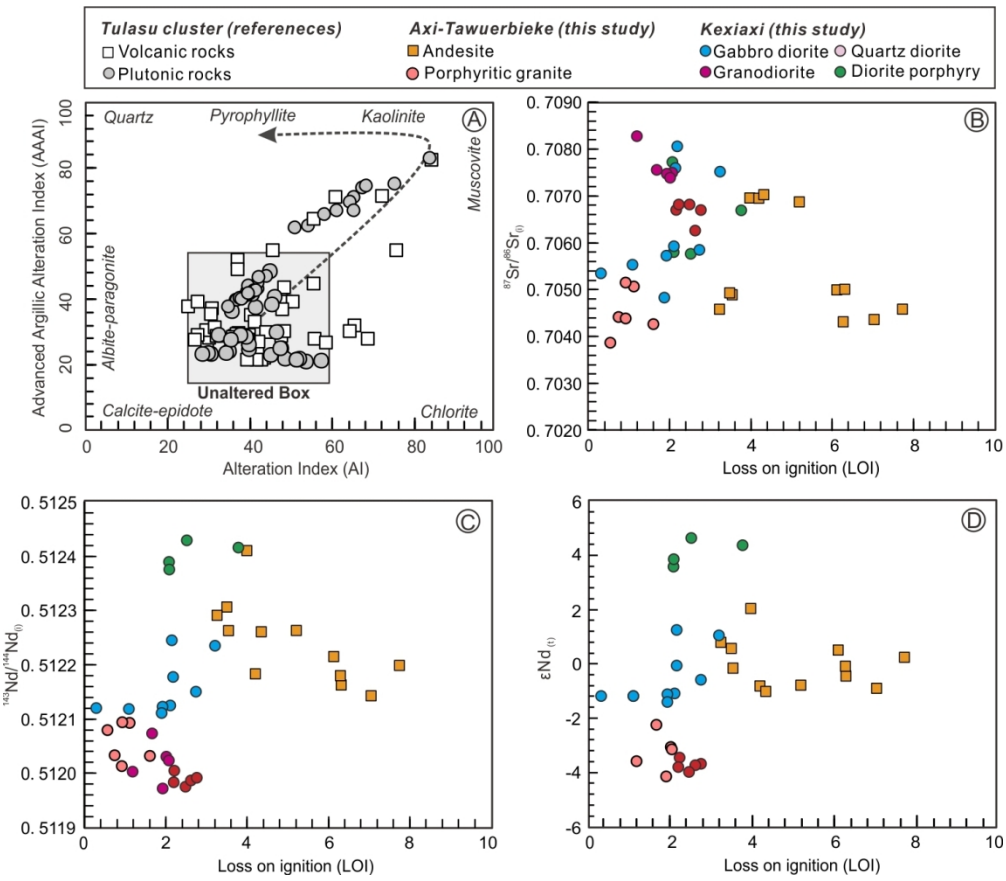

Figure 11. (A) Alteration Box plot (Williams and Davidson, 2004), showing all volcanic and plutonic samples of the Tulasu ore district. Dashed arrow indicates the trend from least altered towards the pyrophyllite alteration zones. The Ishikawa Alteration Index (AI) = 100×[K2O+MgO]/[K2O+MgO+Na2O+CaO], and the Advanced Argillic Alteration Index (AAAI) = 100×Si2O/[Si2O+10×MgO+10×Na2O+10×CaO]. Full datasets see Supplement Table DR2. (B-D) Variation diagrams of loss on ignition (LOI) with 87Sr/86Sr(i), 143Nd/144Nd(i) and εNd(t) for volcanic and plutonic rock samples of the Tulasu district.

128x111mm (300 x 300 DPI)

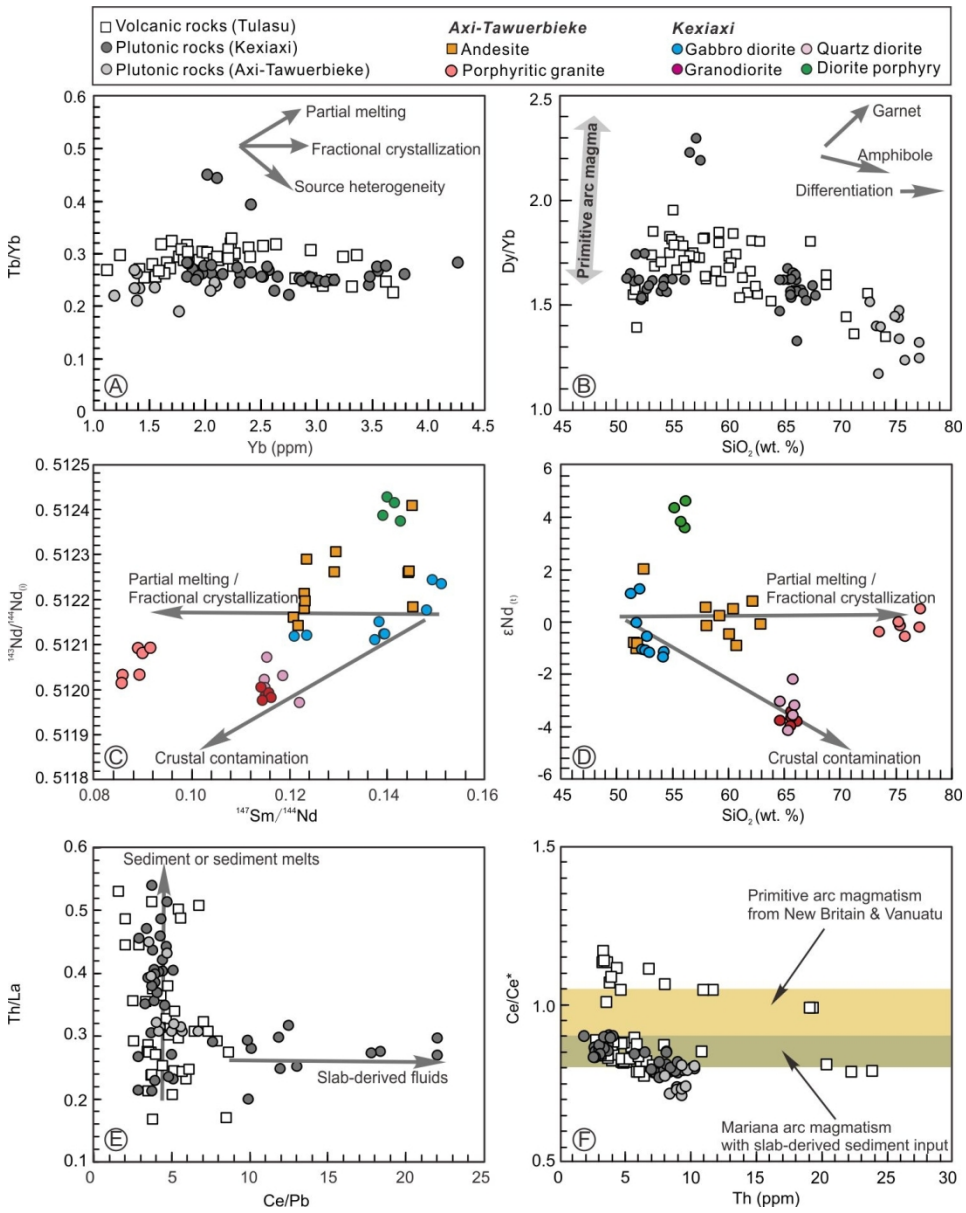

FIGURE 12 Variation diagrams with geochemical trends to discriminate the petrogenetic processes for the volcanic and plutonic rocks of the Tulasu ore district. (A) Yb vs. Tb/Yb (Fan et al., 2004), (B) SiO2 vs. Dy/Yb (Davidson et al., 2007), (C) SiO2 vs. εNd(t), (D) 147Sm/144Nd vs. 143Nd/144Nd, (E) Th/La vs. Ce/Pb and (F) Ce/Ce* vs. Th plots (Hawkins & Ishizuka, 2009)

127x160mm (300 x 300 DPI)

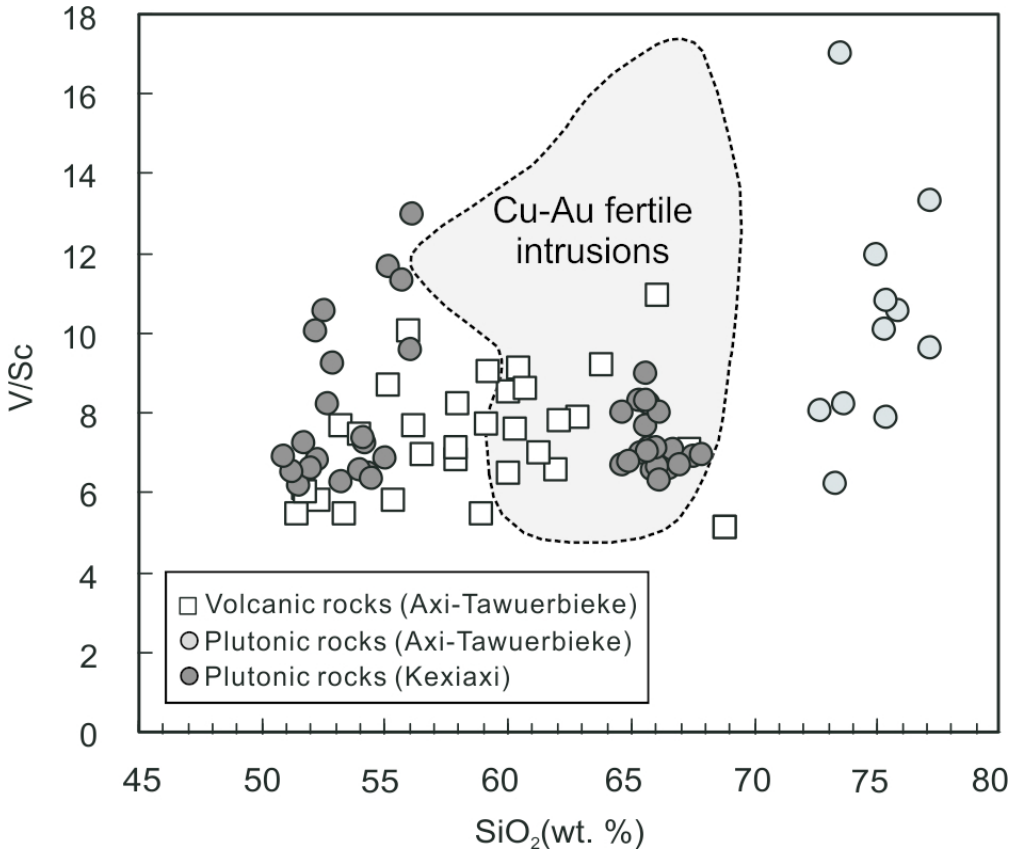

Figure 13. Whole-rock V/Sc vs. SiO2 magma fertility discrimination plot (Loucks, 2014).

79x66mm (300 x 300 DPI)

TABLE 1 Description of the studied volcanic (DVF) and plutonic rock samples of the Tulasu ore district

Lithology	Location	Sample amount (sample No.)	Geological unit	Mineral assemblage (volume percentage)	Whole rock geochemistry	Whole rock $\varepsilon_{Nd}(t)$	T_{DM2} (Ma)	$\varepsilon_{Nd}(t)$ and T_{DM2} references
Andesite	Axi	5 (AX-1, -2, -3, -4, -5)	Uppermost DVF	Phenocryst (15–25%): Pl (10–15%) and Qtz (5–10%); Matrix: Pl and Qtz	this study	-0.9 – +0.5	1062 – 1211	this study
Andesite	Tawuerbieke	3 (TWE-1, -2, -3)	Uppermost DVF	Phenocryst (20–30%): Pl (15–25%) and Qtz (~5%); Matrix: Pl and Qtz, Chl and Ser	this study	-0.2 – +0.8	1050 – 1126	this study
Basaltic andesite	Tawuerbieke	4 (TWE-4, -5, -6, -7)	Uppermost DVF	Phenocryst (15–25%): Pl (10–15%), Amp (2–5%) and Cpx (2–5%); Matrix: Pl, Amp and Fe-Ti oxides	this study	-1.0 – +2.0	949 – 1196	this study
Porphyritic granite	Tawuerbieke	6 (T-10, -11, -12, -13, -14, 15)	Intruded into the uppermost DVF	Phenocryst (15–20%): Pl (8–10%), Kfs (5–10%) and Qtz (3–5%); Matrix: Pl, Kfs and Qtz	Zhao et al. (2014a)	-0.6 – +0.5	1068 – 1155	this study
Gabbro diorite	Kexiaxi	11 (KXX-17, 18, -22, 58, 59, -05, -06, -07, -08, -36, -80)	Intruded into Mesoproterozoic rock	Pl (55–60%), Cpx (12–15%), Amp (10–15%), Bt (5–8%) and minor Fe-Ti oxides	Xue et al. (2013)	-1.3 – +2.3	1007 – 1220	this study
Quartz diorite	Kexiaxi	5 (KXX-12, -29, -30, -31, -32)	Intruded into Mesoproterozoic rock	Pl (50–55%), Amp (15–20%), Qtz (10–15%) and Bt (5–10%)	Xue et al. (2013)	-3.4 – -4.0	1387 – 1433	this study
Granodiorite	Kexiaxi	5 (KXX-01, -02, -34, -35, -37)	Intruded into Mesoproterozoic rock	Pl (40–50%), Kfs (20–25%), Qtz (15–20%) and Bt (5%)	Xue et al. (2013)	-4.2 – -2.2	1285 – 1445	this study
Diorite porphyry	Kexiaxi	4 (KXX-15, -16, -25, -55)	Intruded into Mesoproterozoic rock	Phenocryst (25–35%): Amp (10–15%) and Pl (15–20%); Matrix: Pl and Amp	Xue et al. (2013)	+3.6 – +4.6	726 – 811	this study

Note: Pl–plagioclase; Kfs–K-feldspar; Amp–amphibole; Qtz–quartz; Bt–biotite; Cpx–clinopyroxene; Chl–chlorite; Ser–sericite.

For Peer Review

TABLE 2 Summary of zircon U-Pb ages and Hf isotopes of the volcanic (DVF) and plutonic rocks of the Tulasu ore district

Sample No.	Location	Lithology	Geological unit	Dating method	Age (Ma)	Age reference	$\varepsilon_{Hf}(t)$	T_{DM2} (Ma)	εHf(t) and T_{DM2} reference
AX-2	Axi	Andesite	Uppermost DVF	LA-ICP-MS	351.1 ± 1.8	this study	+2.8 – +12.1	581 – 1174	this study
04 A-5	Axi	Dacite	Uppermost DVF	SHRIMP	363.2 ± 5.7	Zhai et al. (2006)	/	/	/
AX-12	Axi	Andesite	Uppermost DVF	SHRIMP	356.2 ± 2.0	An et al. (2013)	+1.8 – +6.6	990 –1244	An et al. (2017)
TS 26-1	Axi	Andesite	Uppermost DVF	LA-ICP-MS	375.1 ± 3.6	Yu et al. (2015)	/	/	/
06XJ-31	Tawuerbieke	Andesite	Uppermost DVF	LA-ICP-MS	347.1 ± 3.2	Tang et al. (2009)	-5.0 – +7.2	/	Tang et al. (2013)
TWE-20	Tawuerbieke	Andesite	Uppermost DVF	SHRIMP	360.5 ± 3.4	Zhao et al. (2014a)	-0.9 – +10.3	703 –1417	this study
13DT-1	Tawuerbieke	Andesite	Uppermost DVF	LA-ICP-MS	367.1 ± 3.2	Peng et al. (2016)	/	/	/
YM11	Jingxi-Yelmend	Andesite porphyry	Lowermost DVF	SHRIMP	370.5 ± 2.1	An et al. (2014)	-2.0 – +9.2	781 – 1381	An et al. (2017)
JX9	Jingxi-Yelmend	Rhyolite	Lowermost DVF	SHRIMP	386.4 ± 9.3	An et al. (2013)	/	/	/
TWE-35	Tawuerbieke	Porphyritic granite	Intruded into the uppermost DVF	SHRIMP	356.0 ± 4.0	this study	-1.0 – +11.4	446 – 1425	this study
06XJ-34	Tawuerbieke	Porphyritic granite	Intruded into the uppermost DVF	LA-ICP-MS	349.0 ± 2.0	Tang et al. (2013)	-1.7 – +8.2	/	Tang et al. (2013)
TWE-8	Tawuerbieke	Porphyritic granite	Intruded into the uppermost DVF	SHRIMP	355.4 ± 2.3	Zhao et al. (2014a)	+2.6 – +10.2		this study
XT4-8	Tawuerbieke	Monzonite porphyry	Hosted in the uppermost DVF	SHRIMP	356.2 ± 4.3	Zhao et al. (2014b)	/	/	/
KXX-23	Kexiaxi	Gabbroic diorite	Intruded into the uppermost DVF	SHRIMP	357.2 ± 3.0	Xue et al. (2013)	+4.7 – +10.6	687 – 1060	this study
KXX-33	Kexiaxi	Quartz diorite	Intruded into Mesoproterozoic rock	SHRIMP	356.4 ± 2.2	Xue et al. (2013)	+1.6 – +6.9	922 – 1256	this study
KXX-11	Kexiaxi	Granodiorite	Intruded into Mesoproterozoic rock	SHRIMP	350.8 ± 3.8	Xue et al. (2013)	+1.2 – +6.3	955 – 1281	this study
KXX-14	Kexiaxi	Diorite porphyry	Intruded into Mesoproterozoic rock	SHRIMP	348.0 ± 2.2	Xue et al. (2013)	+1.6 – +5.9	963 – 1252	this study
QE21	Kexiaxi	Gabbro diorite	Intruded into Mesoproterozoic rock	SHRIMP	368.0 ± 5.2	Xie et al. (2013)	/	/	/
QE17	Kexiaxi	Granodiorite	Intruded into Mesoproterozoic rock	SHRIMP	354.0 ± 4.1	Xie et al. (2013)	/	/	/

For Peer Review